

Emerging versatile two-dimensional MoSi₂N₄ family

Yan Yin,¹ Qihua Gong*,^{1,2} Min Yi,^{1,*} and Wanlin Guo*¹

¹*Institute for Frontier Science & State Key Lab of Mechanics and Control of Mechanical Structures & Key Lab for Intelligent Nano Materials and Devices of Ministry of Education & College of Aerospace Engineering, Nanjing University of Aeronautics and Astronautics (NUAA), Nanjing 210016, China*

²*MIT Key Lab of Aerospace Information Materials and Physics & College of Physics, Nanjing University of Aeronautics and Astronautics (NUAA), Nanjing 210016, China*

(Dated: October 29, 2022)

The discovery of two-dimensional (2D) layered MoSi₂N₄ and WSi₂N₄ without knowing their 3D parents by chemical vapor deposition in 2020 has stimulated extensive studies of 2D MA₂Z₄ system due to its structural complexity and diversity as well as versatile and intriguing properties. Here, a comprehensive overview on the state-of-the-art progress of this 2D MA₂Z₄ family is presented. Starting by describing the unique sandwich structural characteristics of the emerging monolayer MA₂Z₄, we summarize and anatomize their versatile properties including mechanics, piezoelectricity, thermal transport, electronics, optics/optoelectronics, and magnetism. The property tunability via strain engineering, surface functionalization and layered strategy is also elaborated. Theoretical and experimental attempts or advances in applying 2D MA₂Z₄ to transistors, photocatalysts, batteries and gas sensors are then reviewed to show its prospective applications over a vast territory. We further discuss new opportunities and suggest prospects for this emerging 2D family. The overview is anticipated to guide the further understanding and exploration on 2D MA₂Z₄.

I. INTRODUCTION

Two-dimensional (2D) materials have intrigued great attentions over the years since their fantastic characteristics are close to and even superior than their bulk counterparts, for instance, excellent mechanical properties [1–3], ultrahigh heat conduction [4–6], unique quantum effects in low dimensions (e.g., superconductivity and quantum hall effect, etc.) [7–11]. Since graphene has been successfully prepared by mechanical exfoliation [12–14], most 2D members have been prepared by the top-down exfoliation of their naturally existed bulk parent materials, e.g., mechanical stripping materials (MoS₂, h-BH, NbSe₂, MnBi₂Te₄) [15–17], interface-assisted exfoliation materials (black phosphorene, FeSe, Fe₃GeTe₂, RuCl₃, PtSe₂, PtTe₂, PdTe₂, and CrSiTe₃) [18, 19], and fluid dynamics assisted exfoliation [20–22]. However, their structures are essentially limited by the parent materials. Bottom-up growth method, an another fabrication strategy, has been applied to synthesize dozens of novel 2D materials, e.g., monolayer borophene by direct evaporation [23, 24], multilayer TMDs by chemical vapor deposition (CVD) [25, 26], 2D van der Waals (vdW) heterostructures designed by mechanically assembled stacks [27], and other materials prepared via layer-by-layer stacking in a specific sequence. However, 2D materials synthesized by this method face the challenge of discontinuous growth due to the surface energy constraints.

Recently, Ren and the coworkers successfully prepared novel 2D layer materials (MoSi₂N₄ and WSi₂N₄) without knowing their 3D parents, and broke through the obstacle of island growth [28]. In their growing process, a

Cu/Mo bilayer was used as the substrate and NH₃ gas as the nitrogen source. The crucial point of layer growth by CVD is that the appropriate atomic passivation of surface dangling bonds favors the decrement of surface energy. The growth diagrams of 2D molybdenum nitride without (MoN₂) or with Si (MoSi₂N₄) are shown in Fig. 1(a). The growing progress of MoN₂ without Si shows the obvious island domains and finally uneven micrometer-scale domains (appropriately 10 nm thick) form. On the contrary, MoN₂ with Si (MoSi₂N₄) firstly forms as triangular domains with uniform thickness, then expands to a centimeter-scale uniform polycrystalline film, and eventually maintains great ambient stabilization, as shown in Fig. 1(b). The high-angle annular dark field scanning TEM (HAADF-STEM) observation (Fig. 1(c) and (d)) indicates that MoSi₂N₄ is a MoN₂-derived septuple-atomic-layer compound built up in the order of N-Si-N-Mo-N-Si-N. The vdW form of MoSi₂N₄ can be grown layer by layer due to the free of dangling bonds, indicating the possibility of large-scale preparation of this 2D compound.

Thanks to the breakthrough achievement in experimental synthesis, series of theoretical studies on MoSi₂N₄ and its derived materials have been further carried out. Density functional theory (DFT) calculations define this septuple-atomic-layer compounds as 2D MA₂Z₄ family [29]. This 2D ternary material includes group IVB, VB and VIB elements for M-site atom, group IVA elements for A-site atom and group VA elements for Z-site atom. The general approach to design MA₂Z₄ family layered van der Waals materials is proposed by intercalating MoS₂-type MZ₂ layer into an InSe-type A₂Z₂ monolayer (Fig. 1(e)) [29]. If 2H and 1T phases of MZ₂ and α and β phases of A₂Z₂ are considered, 4 types of monolayer MA₂Z₄ nanosheets can be obtained, i.e., α_i -MA₂Z₄ ($i = 1-6$), β_i -MA₂Z₄ ($i = 1-12$), γ_i -

* yimin@nuaa.edu.cn

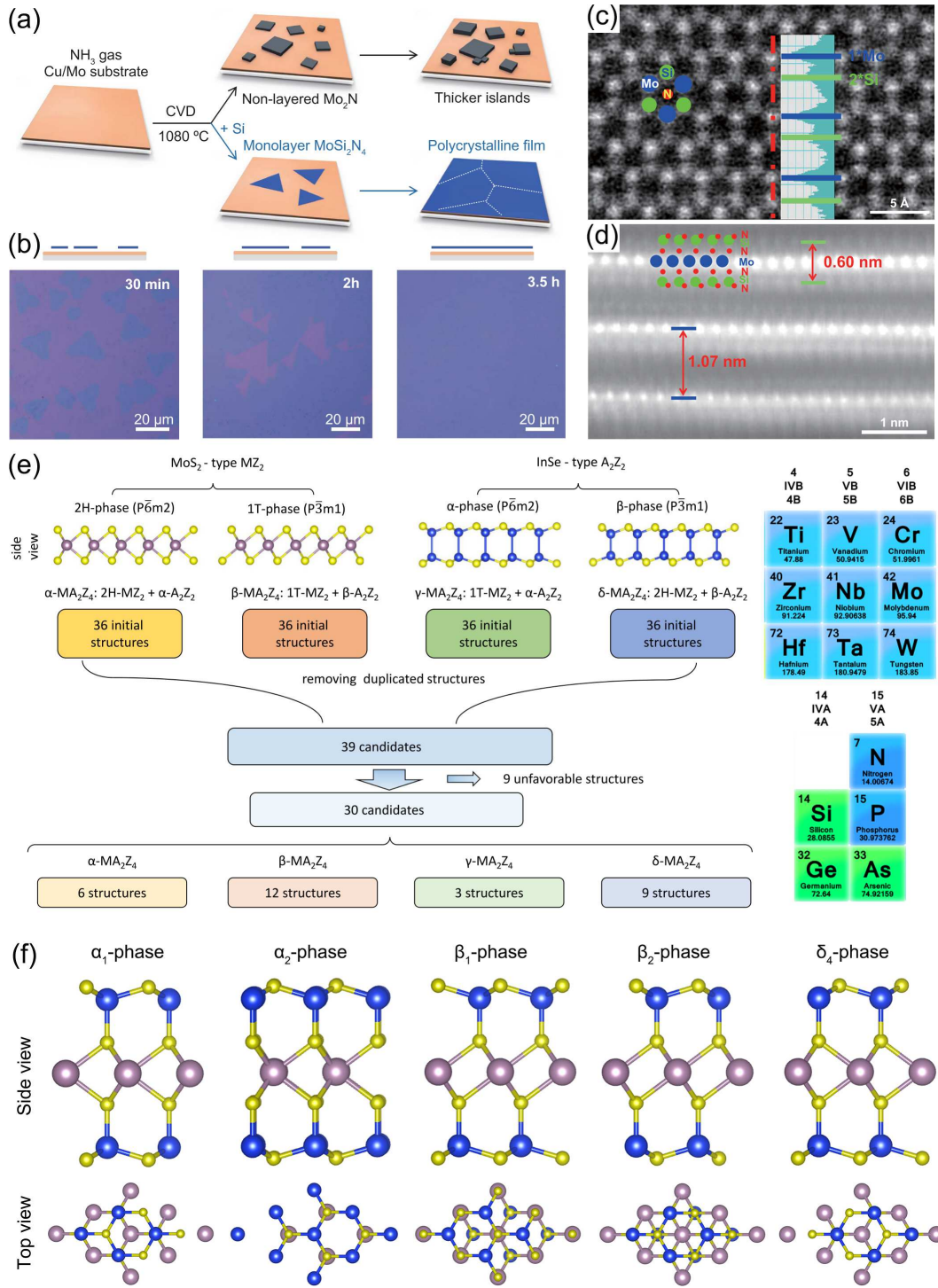


FIG. 1. (a) Growth diagrams of MoN_2 and MoSi_2N_4 by CVD. (b) Optical images of MoSi_2N_4 grown by CVD for 30 min, 2 hours, and 3.5 hours. High-angle annular dark field scanning TEM (HAADF-STEM) imaging: (c) top view and (d) side view. (e) Schematic illustration of the intercalation method that uses the structures of a MoS_2 -like monolayer (2H- and 1T phases) and those of an InSe-like monolayer (α and β phases) to construct the structures of monolayer MA_2Z_4 family. (f) Unit cells for stable 2D MA_2Z_4 with different structures. [28, 29]

MA_2Z_4 ($i = 1-3$) and $\delta_i\text{-MA}_2\text{Z}_4$ ($i = 1-9$). In total, there exist 30 structures of this family by removing duplicate symmetry and abandoning the structures that

are energetically unstable. Five stable structures of 2D MA_2Z_4 are shown in Fig. 1(f). The experimentally synthesized and the most widely studied structure is α_1 -

MA₂Z₄. Due to the rich compositions and diverse structures, MA₂Z₄ family has exhibited intriguing physical and chemical characteristics, such as non-linear optics and second harmonic response [30, 31], quantum behavior of strong exciton-phonon coupling in α_1 -MoSi₂N₄ [32, 33], spin polarization and plasmon properties in α_1 -MoSi₂N₄ [34, 35], superconductivity in α_1 -TaSi₂N₄ and NbSi₂N₄ [36], topological insulating property in β_2 -SrGa₂Se₄ and SrGa₂Te₄ [29], ferromagnetic nature in δ_4 -VSi₂P₄ [29], valley-half-semiconducting property in α_1 -VSi₂N₄ [37], Mott transition in XSi₂N₄ [38], etc. These intriguing properties could enable promising applications of MA₂Z₄ family in nanoelectronic devices such as magnetic tunnel junction, field effect transistors, highly sensitive and reusable gas sensors, etc. [39–46]

In this paper, we aim to review the recent progress of the novel 2D layered MA₂Z₄ family, in terms of its structures, versatile properties and perspective applications. After introducing the diverse structures in Fig. 1, we provide an extensive overview on the versatile properties regarding to mechanics, piezoelectricity, thermal transport, electronics, optics/optoelectronics, and magnetism. The tunability of each property via strain engineering, surface functionalization and layered strategy (e.g., multilayer or heterostructure) is also expounded. Then, we introduce the perspective applications derived from the excellent properties of MA₂Z₄, including transistors, photocatalysts, batteries and sensors. Finally, we summarize the outstanding advantages of this family and suggest the conceivable outlook in the future.

II. VERSATILE PROPERTIES

A. Mechanical properties

Since the extraordinary mechanical properties of graphene (103 GPa of the in-plane stiffness and nearly 1 TPa of the elastic modulus [50]), 2D materials with excellent mechanical properties have attracted great attentions. As for MoSi₂N₄, its experimentally measured tensile strength (E) and elastic modulus (Y) are 65.8 ± 18.3 GPa and 491.4 ± 139.1 GPa [28], respectively, which are nearly half of those in graphene and higher than those in most 2D TMDs (e.g., 22 GPa and 270 ± 100 GPa of MoS₂) [3, 51, 52], MXene (e.g., 17 GPa and 333 GPa of Ti₃C₂T_x [53], 26 GPa and 386 GPa of Nb₄C₃T_x [54]), and black phosphorene [55] (18 GPa and 166 GPa). In detail, Ren et al. [28] measured the mechanical properties of monolayer MoSi₂N₄ via atomic force microscopy nanoindentation (Fig. 2(a)). With a diamond tip of 11.1 nm, the indentation of hole is about 23 nm. The elastic behavior of monolayer MoSi₂N₄ is demonstrated due to the well fitting force-displacement curves of loading and unloading states. Theoretical prediction of mechanical properties of 2D materials is mainly based on the linear elastic model. The theoretically calculated tensile strength and elastic modulus are 48.3–57.8 GPa

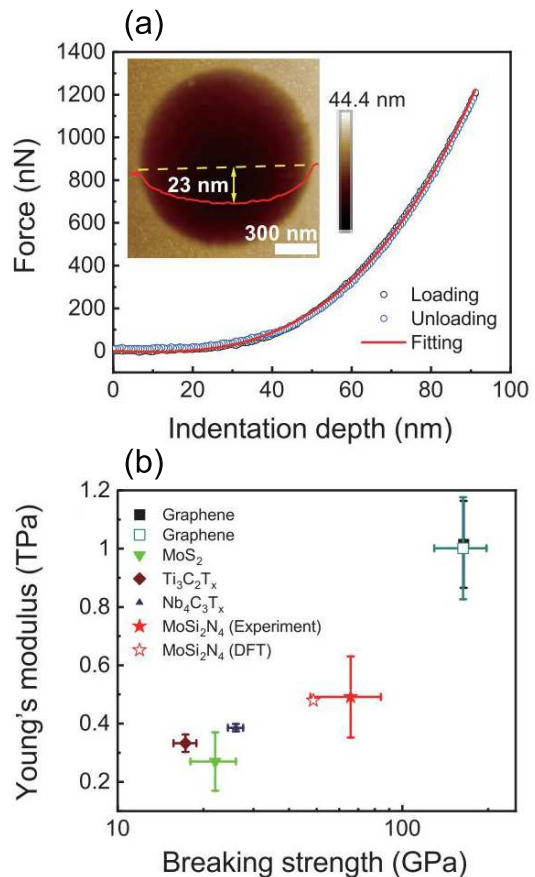


FIG. 2. (a) Force-displacement curve of monolayer MoSi₂N₄ by atomic force microscopy nanoindentation, inset: the nanoindentation profile of suspended MoSi₂N₄. (b) Mechanical properties of MoSi₂N₄ and other 2D materials. [28]

and 479.1–487.0 GPa, respectively [47, 56, 57], in good agreement with experimental values.

Actually, the critical strain and ideal tensile stress of 2D materials are vital indicators for practical applications, which depend on the elastic limit and lattice vibration [58]. Li et al. [56] focused on the elastic limit and failure mechanism of monolayer MoSi₂N₄. Under biaxial and uniaxial (zigzag or armchair) strains, the ideal strengths of monolayer MoSi₂N₄ are similar, about 50 GPa, while the corresponding critical strain is 19.5% (biaxial strain), 26.5% (zigzag strain) and 17.5% (armchair strain). In Fig. 3, when the strains are below 20% ($\epsilon < 20\%$), the tensile stresses (σ) are in the order of $\sigma_{bi} > \sigma_{arm} > \sigma_{zig}$. There exists an obvious yield phenomenon under biaxial and armchair strains when $\epsilon \geq 20\%$, but the yield limit under a zigzag strain is about 25%. By fitting the initial strain-stress curve based on the linear regression up to 1% strain (the inset of Fig. 3(a)), the elastic moduli are calculated as $E_{zig} = 448.3 \pm 5.1$ GPa and $E_{arm} = 457.8 \pm 3.9$ GPa, which are more than twice those of MoS₂ ($E_{zig} = 197.9 \pm 4.3$ GPa and $E_{arm} = 200 \pm 3.7$ GPa) [59]. The degeneracy of elas-

TABLE I. Structures and properties of semiconductors in MA₂Z₄ family: lattice constants (a), bandgap (E_g^{PBE} for PBE and E_g^{HSE} for HSE), carrier mobility (μ_e for electron and μ_h for holes), elastic modulus (Y), tensile strength (E), Poisson's ratio (ν), thermal conductivity (κ). [28, 29, 47–49]

Struc.	Phase	a (Å)	E_g^{PBE} (eV)	E_g^{HSE} (eV)	μ_e (cm ² V ⁻¹ s ⁻¹)	μ_h	Y	E (GPa)	ν	κ (Wm ⁻¹ K ⁻¹)
MoSi ₂ N ₄	α_1	2.91	1.74(Γ -K)	2.31(Γ -K)	200	1000	491.4±139.1 GPa	65.8±18.3	0.28	417–439
MoSi ₂ P ₄	α_1	3.47	0.70(K-K)	0.99(K-K)	246–258	1065–1429	159 GPa	17.5–21.2	*	116–122
	α_2	3.46	0.91(K-K)	1.19(K-K)	*	*	*	*	*	*
MoSi ₂ As ₄	α_1	3.62	0.56(K-K)	0.98(K-K)	*	*	*	*	*	46
	α_2	3.61	0.74(K-K)	1.02(K-K)	*	*	*	*	*	*
MoGe ₂ N ₄	α_1	3.02–3.04	0.91–0.99(Γ K-K)	1.27–1.38(Γ K-K)	490	2190	362 GPa	40.3–42.1	*	286
MoGe ₂ P ₄	α_1	3.55	0.04(Γ -K)	0.84(Γ -K)	*	*	139 GPa	15.3–18.4	*	63
	α_2	3.53	0.56(K-K)	0.95(K-K)	*	*	*	*	*	*
MoGe ₂ As ₄	α_2	3.69	0.47(K-K)	0.83(Γ K-K)	*	*	*	*	*	*
WSi ₂ N ₄	α_1	2.91	2.08(Γ -K)	2.57–2.66(Γ -K)	320	2026	506 GPa	55.5–59.2	0.27	401–503
WSi ₂ P ₄	α_1	3.48	0.53(K-K)	0.81(K-K)	*	*	167 GPa	18.8–22.0	*	129
	α_2	3.46	0.86(K-K)	1.11(K-K)	*	*	*	*	*	*
WSi ₂ As ₄	α_2	3.61	0.71(K-K)	0.95(K-K)	*	*	*	*	*	*
WGe ₂ N ₄	α_1	3.02	1.15–1.29(Γ K-K)	1.51–1.69(Γ K-K)	690	2490	384 GPa	42.6–44.5	*	322
WGe ₂ P ₄	α_1	3.55	0.48(K-K)	0.73(K-K)	*	*	145 GPa	16.5–19.3	*	64
	α_2	3.54	0.63(Γ K-K)	0.89(K-K)	*	*	*	*	*	*
WGe ₂ As ₄	α_2	3.69	0.50(Γ K- Γ K)	0.78(K-K)	*	*	*	*	*	*
CrSi ₂ N ₄	α_1	2.84	0.49(Γ -K)	0.94(K-K)	*	*	468 GPa	55.4–57.8	*	332–348
CrSi ₂ P ₄	α_1	3.42	0.28(K-K)	0.64(K-K)	*	*	154 GPa	18.5–21.2	*	120
	α_2	3.41	0.34(Γ K-K)	0.65(K-K)	*	*	*	*	*	*
CrGe ₂ N ₄	α_1	2.98	0.49(Γ -K)	0.31(Γ -K)	*	*	340 GPa	38.1–38.7	*	198
CrGe ₂ P ₄	α_2	3.49	0.04(Γ K-K)	0.36(Γ K-K)	*	*	*	*	*	*
TiSi ₂ N ₄	α_1	2.93	1.57(Γ M-M)	2.50(Γ M-M)	*	*	*	*	*	107
ZrSi ₂ N ₄	α_1	3.04	1.55(Γ M-M)	2.41(Γ M-M)	*	*	382 N/m	*	0.32	82
	β_2	3.05	1.00(Γ -M)	0.36(Γ -M)	*	*	400 N/m	*	0.26	*
ZrGe ₂ N ₄	β_2	3.19	1.04(Γ - Γ)	2.34(Γ - Γ)	*	*	*	*	*	*
HfSi ₂ N ₄	α_1	3.02	1.80(Γ M-M)	2.70(Γ M-M)	*	*	406 N/m	*	0.32	124
	β_2	3.04	1.21(Γ -M)	2.21(Γ -M)	*	*	420 N/m	*	0.25	*
HfGe ₂ N ₄	β_2	3.18	1.15(Γ - Γ)	2.45(Γ - Γ)	*	*	*	*	*	*
PdSi ₂ N ₄	β_2	2.99	2.50(Γ -M)	3.80(Γ -M)	*	*	356 N/m	*	0.29	*
PtSi ₂ N ₄	β_2	3.02	2.50(Γ -M)	3.80(Γ -M)	*	*	349 N/m	*	0.30	*

tic moduli indicate a nearly elastic isotropy in monolayer MoSi₂N₄. On the other hand, the failure mechanism has been investigated on the aspect of lattice stability by phonon dispersion. When the tensile strength limit is reached under an armchair strain, the phonon dispersion has no imaginary frequency. This indicates lattice stability and further reveals that the failure phenomenon of

monolayer MoSi₂N₄ is ascribed to the elastic failure of the SiN layer before reaching the critical strain. The obvious imaginary frequency of out-of-plane acoustic branch (ZA) before reaching tensile strength limit demonstrates that the failure mechanism of monolayer MoSi₂N₄ is attributed to phonon instability under the zigzag or biaxial strains.

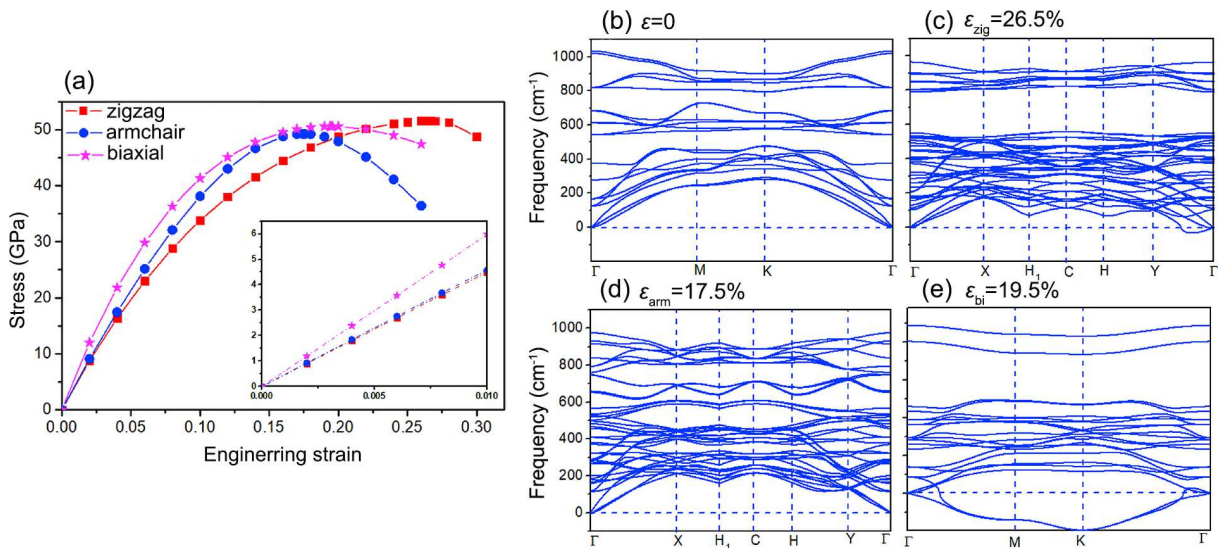


FIG. 3. (a) Strain-stress curve of monolayer MoSi_2N_4 and the corresponding phonon dispersion under different strains: (b) no strain, (c) zigzag uniaxial strain $\epsilon_{\text{zig}} = 26.5\%$, (d) armchair uniaxial strain $\epsilon_{\text{arm}} = 17.5\%$, (e) biaxial strain $\epsilon_{\text{bi}} = 19.5\%$. [56]

The mechanical parameters of other members in MA_2Z_4 family are listed in Table 2. Mortazavi et al. [47] found in MA_2Z_4 family the mechanical properties are mainly affected by the terminating atom (Z-site) rather than the core atom (M-site). Three possible factors that influence the mechanical properties are proposed: Z-site atomic mass, structure and chemical bonds. Firstly, increasing Z-site atomic weight deteriorates the mechanical properties, but the elastic modulus has little change when M-site atomic mass is increased. For examples, MA_2N_4 has higher Y and E than MA_2P_4 , while Y and E of MoSi_2N_4 and WSi_2N_4 are close. Secondly, since the M-A bonds are absolutely vertical, only M-Z and A-Z bonds participate in the deformation when applying an in-plane loading, indicating that the two bonds related to Z-site atoms determine the mechanical properties. Besides, chemical bonds formed with N atoms are always stronger than those with P/As atoms. Bonds formed with Si are sturdier than those with Ge, resulting in the highest elastic modulus of monolayer MSi_2N_4 .

The mechanical properties of some other MA_2Z_4 -derived materials have also been investigated, e.g., CrC_2N_4 , SnSi_2N_4 , SnGe_2N_4 and XMoSi_2N_2 ($X = \text{S}/\text{Se}/\text{Te}$) [60–63]. The predicted elastic modulus and tensile strength of CrC_2N_4 are as high as 676 and 54.8 GPa, respectively, while those of SnSi_2N_4 (478 and 47 GPa) are close to those of MoSi_2N_4 . This indicates that the MA_2Z_4 structure offers excellent mechanical features, but the intrinsic mechanisms related to the elements and structures require further studies.

B. Piezoelectricity, ferroelectricity and flexoelectricity

Piezoelectricity of 2D materials can convert mechanical energy into electrical energy and *vice versa*, which always occurs in semiconductors or insulators with broken inversion symmetry. The relaxation piezoelectric coefficients (e_{ijk} and d_{ijk}) are expressed as

$$e_{ijk} = \frac{\partial P_i}{\partial \epsilon_{jk}} = e_{ijk}^{\text{elc}} + e_{ijk}^{\text{ion}} \quad (1)$$

and

$$d_{ijk} = \frac{\partial P_i}{\partial \sigma_{jk}} = d_{ijk}^{\text{elc}} + d_{ijk}^{\text{ion}} \quad (2)$$

where P_i , ϵ_{jk} , σ_{jk} are polarization vector, strain and stress. The subscript *elc* or *ion* represent the electronic or ionic contributions. The relationship between d_{ijk} and e_{ijk} is built via elastic tensor (C_{ij} , with the Voigt notation). The independent parameters of tensor are reduced due to the symmetry of crystal structure. In monolayer MA_2Z_4 , the counterpart with $P\bar{6}m2$ space group prohibits the out-of-plane piezoelectric effect, so that only the in-plane piezoelectric strain and stress coefficients (i.e., e_{11} , d_{11}) and elastic coefficients (i.e., C_{11} , C_{12}) are considered [64, 65].

Structure effect on piezoelectricity of MA_2Z_4 has been investigated [64]. The structures are divided into six configurations by different operations (translation, mirror and rotation) of A_2Z_2 layers, which are nominated as α_i ($i = 1-6$), as shown in Fig. 4(a). It is observed that the values of $C_{11} - C_{12}$ of MSi_2N_4 ($M = \text{Mo}, \text{W}$) are close when $i = 1, 2, 4, 5$, while those of $C_{11} - C_{12}$ are higher when $i = 3, 6$, indicating α_3 and α_6 MSi_2N_4 ($M = \text{Mo}/\text{W}$) with high resistance to deformation. The

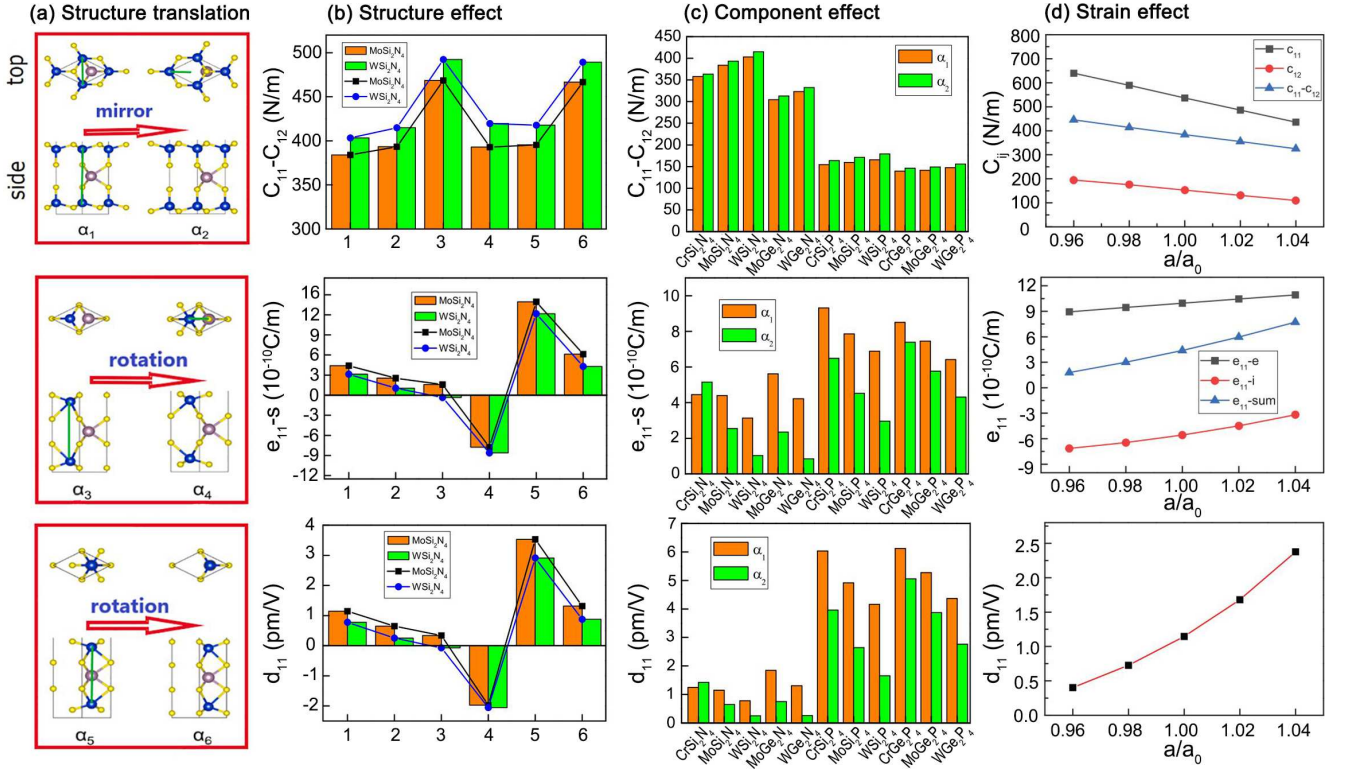


FIG. 4. (a) Structure translation of α_i -MA₂Z₄ ($i = 1-6$). (b-d) Structure, component and strain effects on piezoelectric parameters. [64, 65]

structural sensibility of d_{11} is homologous with that of e_{11} from α_1 to α_6 . e_{11} of α_5 exhibits the largest value among six structures, which is 13.95×10^{-10} C/m for MoSi₂N₄ and 12.17×10^{-10} C/m for WSi₂N₄. d_{11} of α_5 -MoSi₂N₄ and α_5 -WSi₂N₄ is 3.53 and 2.91 pm/V, respectively. d_{11} of α_1 -MoSi₂N₄ and α_1 -WSi₂N₄ (experimentally synthesized phases) is 1.15 and 0.78 pm/V, respectively.

Studies on the influence of different M/A/Z atoms reveal that $C_{11} - C_{12}$ of both α_1 and α_2 improves with the element periodicity increasing (Fig. 4(c)). For instance, $C_{11} - C_{12}$ of MSi₂N₄ is in the order of CrSi₂N₄ > MoSi₂N₄ > WSi₂N₄. The larger elastic constants of MA₂N₄, compared with those of MA₂P₄ and other 2D materials (e.g., TMDs, metal oxides, and III-V semiconductors [66, 67]), indicate that MA₂N₄ system is more rigid. The change trend of e_{11} and d_{11} follows the opposite regularity, compared with elastic coefficients. d_{11} of MA₂P₄ with the same M and A atoms is larger than that of MA₂N₄ for both α_1 and α_2 phases. d_{11} of α_1 - and α_2 -MA₂Z₄ is in the range of 0.78–6.12 pm/V and 0.25–5.06 pm/V, respectively. Monolayer MA₂P₄ nanosheets (e.g., α_1 -CrSi₂P₄, α_1 -MoSi₂P₄, α_1 -CrGe₂P₄, α_1 -MoGe₂P₄ and α_2 -CrGe₂P₄) show excellent piezoelectric response. In addition, the effect of A-site atoms on piezoelectric performance can be ignored so that d_{11} of MoGe₂N₄ is close to that of MoSi₂N₄. d_{11} of most monolayer MA₂P₄ nanosheets is even larger than that of 2D TMDs (e.g., $d_{11} = 3.65$ pm/V of MoS₂, $d_{11} = 2.12$ pm/V

of WS₂, $d_{11} = 4.55$ pm/V of MoS₂, and $d_{11} = 2.64$ pm/V of WSe₂) [68] and d_{33} (3.1 pm/V) of bulk piezoelectric wurtzite GaN [69].

The compressive and tensile biaxial strain are shown to obviously improve and deteriorate the piezoelectric performance of MoSi₂N₄, respectively (Fig. 4(d)) [65]. Piezoelectric stress and strain responses are improved with the in-plane strain from -4% to 4%. d_{11} can be enhanced by 107% if a tensile biaxial strain of 4% is applied. VSi₂P₄, a spin-gapless semiconductor (SGS), possesses a wide range of properties due to its strain sensitivity. With the increasing strain, it presents as ferromagnetic metal (FMM), SGS, ferromagnetic semiconductor (FMS), or ferromagnetic half-metal (FMHM) [70]. In the strain range of 1%–4%, the coexistence of ferromagnetism and piezoelectricity can be achieved in FMS VSi₂P₄. Its d_{11} under 1%, 2% and 3% strain is 4.61, 4.94 and 5.27 pm/V, respectively.

There exist both in-plane and out-of-plane piezoelectric polarizations in Janus MSiGeN₄ (M = Mo/W) owing to the broken reflection symmetry along the out-of-plane direction [71, 72]. The in-plane piezoelectric coefficients of Janus MSiGeN₄ ($d_{11} = 1.494$ pm/V for MoSiGeN₄, $d_{11} = 1.050$ pm/V for WSiGeN₄) are between those of MSi₂N₄ and MGe₂N₄, while the out-of-plane stress piezoelectric coefficients (d_{31}) are -0.014 and 0.011 pm/V for MoSiGeN₄ and WSiGeN₄, respectively. Under an in-plane biaxial strain, d_{11} of MSiGeN₄ is improved with

the increasing e_{11} , which is similar with MA_2N_4 . A tensile strain of 10% can increase d_{11} of MoSiGeN_4 and WSiGeN_4 by several times, with the values up to 8.081 and 7.282 pm/V, respectively. On the contrary, a compressive biaxial strain can effectively enhance the out-of-plane piezoelectric response. The MA_2Z_4 -derived SrAlGaSe_4 has both in-plane ($d_{11} = -1.865$ pm/V) and out-of-plane ($d_{31} = -0.068$ pm/V) piezoelectricity under uniaxial a tensile strain of 6% [73].

In addition to piezoelectricity, the intrinsic ferroelectricity and its electrical switching in MA_2Z_4 are still open issues. For example, the sliding ferroelectricity is found in vdW MoA_2N_4 bilayer and multilayer [74]. The interlayer inequivalence caused by the stacking order directly generates the out-of-plane polarization. Then, the induced vertical polarization can be switched via the interlayer sliding. The calculated vertical polarization is 3.36, 3.05, 2.49 and 3.44 pC/m for AB stacking bilayer MoSi_2N_4 , MoGe_2N_4 , CrSi_2N_4 and WSi_2N_4 , respectively, which are higher than that of bilayer WTe_2 and BN [75, 76].

The flexoelectricity of monolayer MA_2Z_4 is also of interest, which is often induced by bending deformation of 2D materials with a strain gradient [47]. The out-of-plane bending flexoelectric coefficients of 12 kinds of MA_2Z_4 ($\text{M} = \text{Mo}/\text{Cr}/\text{W}$, $\text{A} = \text{Si}/\text{Ge}$, $\text{Z} = \text{N}/\text{P}$) are found in the range of 0.001–0.047 nC/m under a bending strain gradient of $0.3/\text{\AA}$. The highest flexoelectric coefficient of WGe_2N_4 is about 1.5 times higher than that of MoS_2 [77]. It is proposed that the enhancement of flexoelectricity is insufficient with the bending deformation, but is broadened by the construction of asymmetry structures (e.g., Janus counterparts) [78, 79].

C. Thermal conductivity

Owing to the high tensile strength and thus strong bond interactions, the thermal conductivity of monolayer MA_2Z_4 family has attracted attentions. Based on thermal Boltzmann transport equations, the theoretical lattice thermal conductivity (κ) of MoSi_2N_4 is predicted as high as $400 \text{ Wm}^{-1}\text{K}^{-1}$ at room temperature [47, 49, 80, 81], which is larger than that of most other 2D materials, such as hydrogenated borophene ($368 \text{ Wm}^{-1}\text{K}^{-1}$) [82], TMDs ($23\text{--}142 \text{ Wm}^{-1}\text{K}^{-1}$) [83–85], group IVA and VIA compounds ($0.26\text{--}9.8 \text{ Wm}^{-1}\text{K}^{-1}$) [86, 87]. But it is lower than that of graphene ($3000\text{--}5000 \text{ Wm}^{-1}\text{K}^{-1}$) [88, 89], and h-BNs ($600 \text{ Wm}^{-1}\text{K}^{-1}$) [90]. Such high thermal conductivity of monolayer MoSi_2N_4 is promising for heat conductors and thermal management in semiconductor devices.

In Slack's classic rules [91, 92], crystals with high thermal conductivity follows four rules: simple crystal structure, light atomic masses, strong bonding and low anharmonicity. In the monolayer MA_2Z_4 family, by replacing M/A/Z atoms at different sites, the different contributions to κ have been further examined [47, 49]. It is found that when Z- site atoms are replaced, κ

of monolayer MA_2Z_4 obeys the Slack's rules (red lines in Fig. 5(a)). For instance, κ of MoSi_2Z_4 decreases by one order of magnitude from Z = N to As, indicating that Z atom plays a critical role in controlling the thermal conductivity of MoSi_2Z_4 . The similar variation phenomena are found in MoGe_2Z_4 and WGe_2Z_4 as well. Meanwhile, in A-site-replaced MA_2Z_4 , κ is decreased by about 40.3%–50.4% from A = Si to Ge. κ of MoGe_2N_4 ($286 \text{ Wm}^{-1}\text{K}^{-1}$) is about 40.3% lower than that of MoSi_2N_4 ($439 \text{ Wm}^{-1}\text{K}^{-1}$). κ of WGe_2P_4 ($64 \text{ Wm}^{-1}\text{K}^{-1}$) is only half that of WSi_2P_4 ($129 \text{ Wm}^{-1}\text{K}^{-1}$). The decreasing phenomena are intrinsically attributed to the phonon properties. The Z- or A-site atoms of MA_2Z_4 determine the phonon frequency range. Monolayer MA_2N_4 shows wider frequency range than MA_2P_4 and MA_2As_4 (Fig. 5(b)). MSi_2Z_4 exhibits wider phonon dispersion than MGe_2Z_4 . Thermal conductivity is related to the phonon group velocity that directly depends on phonon branches. Thus, wider phonon bands lead to higher phonon group velocity and result in higher thermal conduction.

When M atoms are from different group IVB or VIB atoms, the variation of κ is abnormal and the conventional guideline for searching high κ does not work. κ exhibits an irregular oscillation with the increasing atomic mass and decreasing Debye temperature (green dash lines in Fig. 5(a)). Mortazavi et al. proposed that the weight of core atoms is the dominant factor on thermal conduction of MA_2Z_4 and κ increases with the weight of core atoms. This violates the Slack's rules but is consistent with the classical theory that stiffer systems favor a higher κ . However, in our recent work [49], we found that the influential factors on the variation of κ is not limited to the atomic mass. For instance, the average mass of WSi_2N_4 is 1.5 times that of CrSi_2N_4 , but κ shows only 13% difference. We proposed that the abnormal thermal conductivity of M-site replaced MA_2Z_4 is relative to the group that M atoms belong to. κ of MA_2Z_4 with group VIB M atom is about 3–4 times of that with group IVB M atom. These abnormal phenomena with respect to M atoms are attributed to the fundamental vibrational properties and phonon scattering behavior. The acoustic branches of MA_2Z_4 with group VIB M are more bunched and less flattened. Consequently, the phonon scattering rates (Fig. 5(c)) of group VIB M-site MA_2Z_4 are lower than that of group IVB M-site MA_2Z_4 , and higher κ presents in the former. As shown in Fig. 5(d), the thermal conductivity of monolayer MA_2Z_4 family is in a very wide range ($10^1\text{--}10^3 \text{ Wm}^{-1}\text{K}^{-1}$), locating between that of 2D TMDs and hBN.

D. Thermoelectric properties

In addition to the thermal conductivity, the thermoelectric performance of monolayer MA_2Z_4 has been also investigated. The dimensionless figure of merit (ZT) is always used to measure the efficiency of thermoelec-

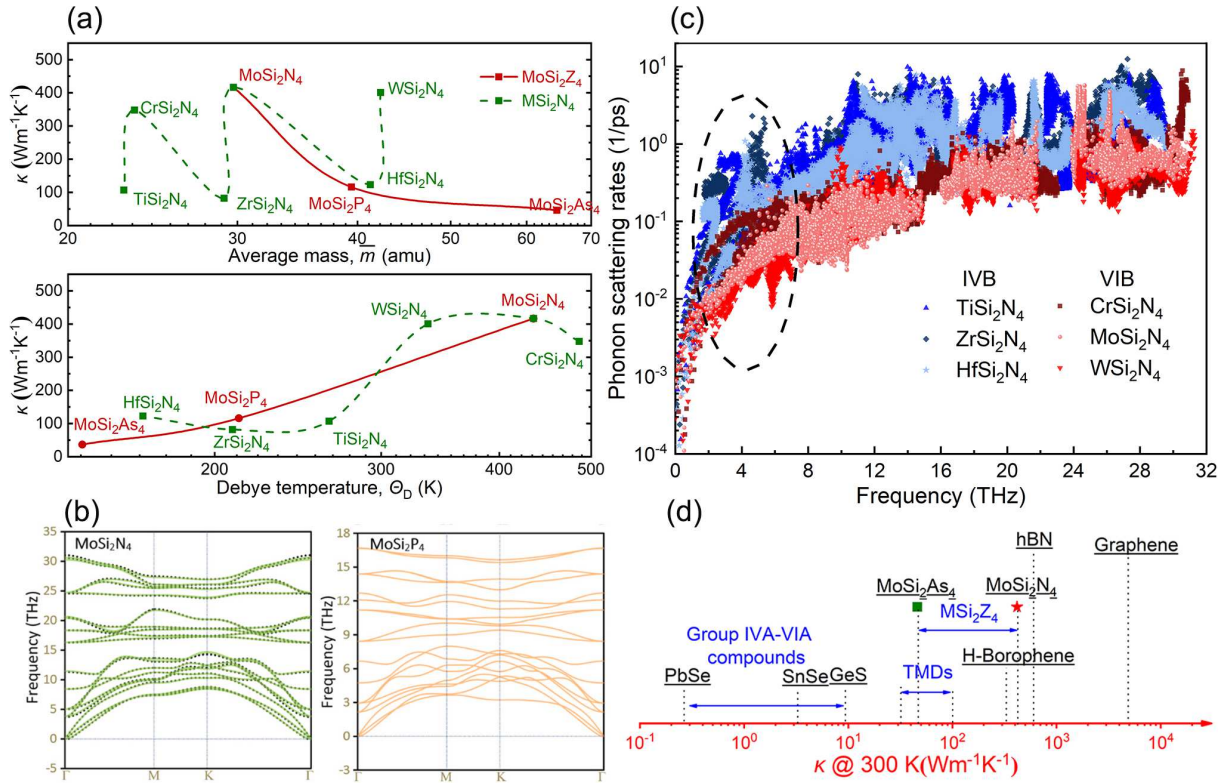


FIG. 5. (a) Thermal conductivity (κ) as a function of average mass (upper) and Debye temperature (down). (b) Phonon dispersion of MoSi₂N₄ and MoSi₂P₄, where the frequency range of MoSi₂N₄ is wider than that of MoSi₂P₄. (c) Phonon scattering of MA₂Z₄ with different M-site atoms, indicating that MA₂Z₄ with group VIA atom has lower scattering rates. (d) Comparison of κ at 300 K between MA₂Z₄ family and other 2D materials. [47, 49]

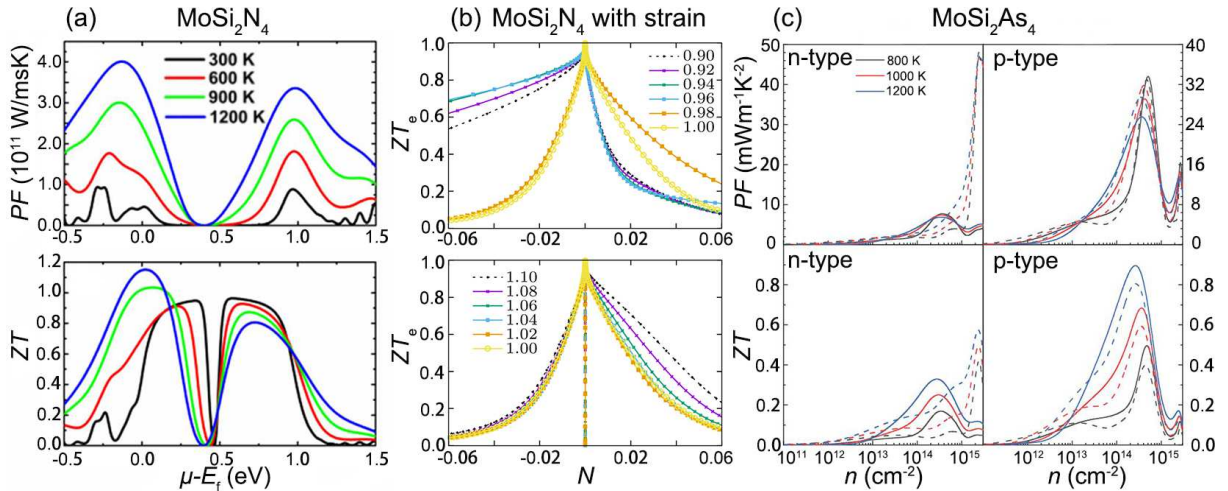


FIG. 6. (a) Thermoelectric performance of monolayer MoSi₂N₄ at different temperatures: Power factor (PF) (top) and figure of merit (ZT) (bottom). (b) Effect of compressive (top) and tensile (bottom) strain on ZT . (c) Thermoelectric performance of monolayer MoSi₂As₄. [57, 93, 94]

tric conversion of a thermoelectric material, which is expressed as:

$$ZT = \frac{S^2 T}{\rho(\kappa_e + \kappa_l)} \quad (3)$$

where S , $1/\rho$, T , κ_e , and κ_l are the Seebeck coefficient, electrical conductivity, working temperature, electronic thermal conductivity and lattice thermal conductivity, respectively. The higher ZT indicates the better heat-to-electricity conversion efficiency. Thus, 2D materials

for the thermoelectric field are prone to semiconductors with high Seebeck coefficient, electrical conductivity and low thermal conductivities.

The power factor ($PF = S^2T/\rho$) of monolayer MoSi_2N_4 is studied to evaluate the capability of producing electricity [57]. The heat conversion into electricity is favored by the temperature since PF increases considerably with temperature. The maximum PF is located at a chemical potential range of 0.12–0.98 eV (upper in Fig. 6(a)). PF in the negative chemical potential region is more sensitive to temperature than in the positive region. Meanwhile the maximum ZT increases with temperature in the chemical potential range of -0.45–0.5 eV. The maximum ZT of monolayer MoSi_2N_4 is up to 1.2 at 1200 K [57], while ZT of MoGe_2N_4 is up to 1.0 at 900 K [95]. Guo et al. [93] studied the effect of strain on the thermoelectric performance of monolayer MoSi_2N_4 , as shown in Fig. 6(b). They found that the compressive strain rather than the tensile strain has significant effect on S . Besides, S with n-type doping has observable improvement under a compressive strain, which is ascribed to the strain-driven conduction band degeneracies.

As mentioned above, the high lattice thermal conductivity of monolayer MoSi_2N_4 brings negative effect on ZT and further restrains the thermoelectric performance. It is imperative for seeking other MA_2Z_4 semiconductors with low thermal conductivity to satisfy the requirement of high ZT . Monolayer MoSi_2As_4 semiconductor has no doubt to be a good candidate due to its low lattice thermal conductivity. However, Huang et al. [94] found that ZT of MoSi_2As_4 is 0.33 for n-type and 0.90 for p-type at 1200 K, which are even lower than that of MoSi_2N_4 (Fig. 6(c)). The underlying reason still remains unknown. Hence, whether there is any member with ultra-high thermoelectric properties needs to be further explored.

E. Electrical properties

Till now, nearly hundred members in monolayer MA_2Z_4 family have been predicted. Wang et al. [29] systematically investigated 72 thermodynamically and dynamically stable MA_2Z_4 compounds with a septuple-atomic-layer which possess the same intercalated architecture as MoSi_2N_4 . The electric properties can be classified according to the total numbers of valence electrons. Most of monolayer MA_2Z_4 nanosheets with 32 or 34 valence electrons are semiconductors, while those with 33 valence electrons are non-magnetic metals or ferromagnetic semiconductors. Ding et al. [98] identified 12 stable MSi_2N_4 with trigonal prismatic (H-phase) or octahedral (T-phase) structures, including six new members. The M-site atoms contain both the early transition metal element (group IIIB–VIB) and the late transition metal (group VIIIB, e.g., Pd and Pt). Group IIIB and IVB MSi_2N_4 with H- and T-phase geometries are all stable, while group VB and VIB ones are only stable with

H-phase. Moreover, other MoSi_2N_4 derived structures have emerging in an overwhelming trend, such as, bilayer or multilayer MA_2Z_4 , heterostructures, Janus MA_2Z_4 , etc. These MA_2Z_4 nanosheets exhibit versatile electronic properties depending on the number of valence electrons and structural phases. In this subsection, we emphatically discuss the intrinsic electrical properties of these monolayers and their tunability.

H-phase monolayer MA_2Z_4 nanosheets, where $M = \text{Cr/Mo/W/Ti/Zr/Hf}$, $A = \text{Si/Ge}$, $Z = \text{N/P/As}$, are semiconductors with a bandgap around 0.04–1.79 eV (PBE) and 0.31–2.57 eV (HSE) calculated by DFT [47, 49]. Monolayer MA_2N_4 nanosheets are indirect bandgap materials (Γ -K), while monolayer MA_2P_4 nanosheets are direct gap semiconductors (K-K). The electronic contribution to CB and VB derived primarily from interior atomic orbitals leads to the robust band edge states [99]. From the projected band structure and charge density distribution (Fig. 7), valence band maximum (VBM) at Γ point is mainly contributed by M- d_{z^2} orbital and marginally contributed by Z- p_z and A- p_z , while at K point it is contributed by M- $(d_{x^2-y^2}, d_{xy})$ and Z- (p_x, p_y, p_z) orbitals which locate at the centre area of the structure. Conduction band minimum (CBM) is solely occupied by M- (s, d_{z^2}) orbitals. The strong interaction of d orbitals of M atom renders to the highly dispersion between VB and CB, indicating high charge carrier mobilities and small effective masses. The calculated electron and hole mobilities are 200 and 1100 $\text{cm}^2\text{V}^{-1}\text{s}^{-1}$ for MoSi_2N_4 , 490 and 2190 $\text{cm}^2\text{V}^{-1}\text{s}^{-1}$ for MoGe_2N_4 , 320 and 2026 $\text{cm}^2\text{V}^{-1}\text{s}^{-1}$ for WSi_2N_4 , 690 and 2490 $\text{cm}^2\text{V}^{-1}\text{s}^{-1}$ for WGe_2N_4 [47]. The carrier mobility (μ) of monolayer MoSi_2P_4 is comparable with that of MoSi_2N_4 , where μ in zigzag (armchair) direction is 245.992 (257.985) $\text{cm}^2\text{V}^{-1}\text{s}^{-1}$ for electrons and 1065.023 (1428.885) $\text{cm}^2\text{V}^{-1}\text{s}^{-1}$ for holes [48], which are much higher than those of MoS_2 (72.16 and 200.52 $\text{cm}^2\text{V}^{-1}\text{s}^{-1}$ [100]). Besides, SnGe_2N_4 [62], a MA_2Z_4 -derived structure without transition metals, possesses a high electron mobility of 1061.66 $\text{cm}^2\text{V}^{-1}\text{s}^{-1}$, but a low hole mobility of 28.35 $\text{cm}^2\text{V}^{-1}\text{s}^{-1}$, owing to a strongly concave downward conduction band and a flat valence band. Recent DFT calculations also indicate 2D MoSi_2N_4 as an ideal platform for the exploration of exciton-involved physics [101].

The bandgap of bilayer MoSi_2Z_4 ($Z = \text{P/As}$) is similar with that of monolayers due to the weak vdW interaction between layers. In terms of carrier mobilities, there exist several interesting phenomena [102]. (1) In monolayer and bilayer MoSi_2Z_4 , the hole carrier mobilities are about 3–4 times larger than those of electrons. The difference of carrier mobilities effectively facilitates the spatial separation of electrons and holes, restraining the recombination probability of photo-excited carriers. (2) Carrier mobility of bilayer MoSi_2Z_4 , especially hole carrier mobility, exhibits anisotropic behaviors. (3) the carrier mobilities (electron and hole) of bilayer MoSi_2Z_4 are about 2 times that of monolayer MoSi_2Z_4 . Mono-

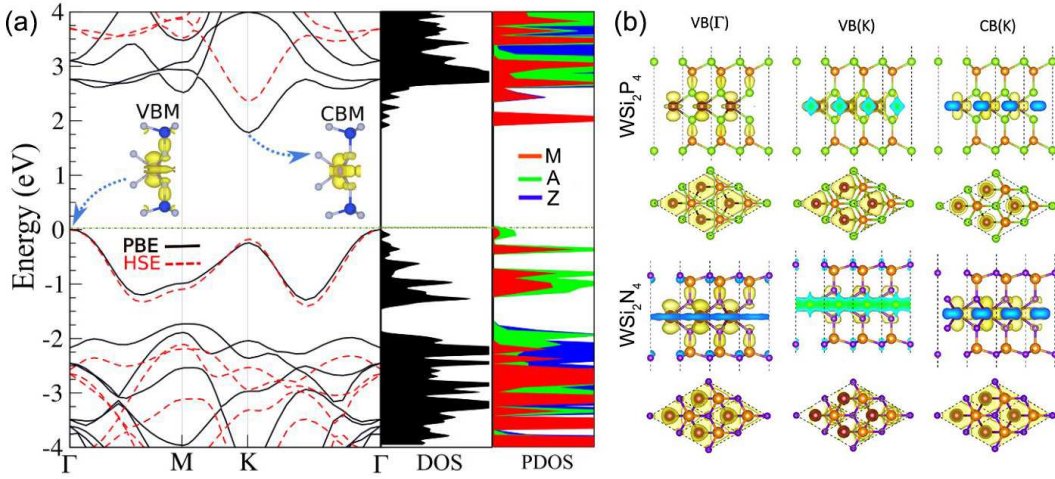


FIG. 7. (a) Band structure of monolayer MoSi_2N_4 . (b) Charge density distribution of WSi_2P_4 and WSi_2N_4 at $\text{VB}(\Gamma)$, $\text{VB}(\text{K})$ and $\text{CB}(\text{K})$ with the isosurface value as $0.01 \text{ e}/\text{\AA}^3$. [47, 57]

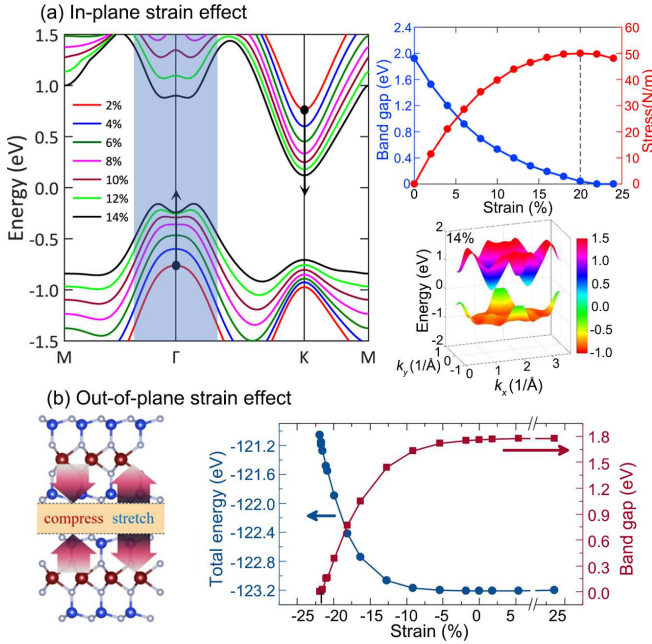


FIG. 8. (a) In-plane strain effect on monolayer MoSi_2N_4 : variation of band structure (left), bandgap and stress versus strain (top right), and 3D ‘Mexican hat’ band under a tensile strain of 14% (bottom right). (b) Out-of-plane strain effect on bilayer MoSi_2N_4 . [96, 97]

layer and bilayer MoSi_2Z_4 with high carrier mobilities exhibit pronounced carrier polarization and are promising materials for high-performance nanoscale electronic and optoelectronic devices.

The electronic transition of monolayer MA_2Z_4 from semiconductor to metal can be triggered by applying in-plane strains [48, 96]. The bandgap of monolayer MoSi_2N_4 decreases with the increasing in-plane biaxial strain (Fig. 8(a)). The relation between bandgap (E_g)

and strain (ϵ) is fitted as [96] $E_g = 0.004 \epsilon^2 - 0.17 \epsilon + 1.87$. Under an in-plane biaxial strain of 4% (6%), the effective mass of holes is $-2.33 m_e$ ($-3.84 m_e$) and the effective mass of electrons is $0.48 m_e$ ($0.43 m_e$). This suggests that the in-plane biaxial strain simultaneously enhances the localization of holes and free electrons, which would achieve fascinating features like ferromagnetism and superconductivity. When the in-plane strain is over 10%, there exists an inversion at the edge of VBM, known as a ‘Mexican hat’ in which two VBMs are induced and the transport properties would be improved. As the strain increases, the variation of ‘Mexican hat’ dispersion is more noticeable. When $\epsilon = 20\%$, MoSi_2N_4 becomes semimetal. For MoSi_2P_4 under an in-plane armchair strain, the bandgap transfers to be indirect at $\epsilon = 2\%$, 3% and returns to be direct at $\epsilon = -10\%$ [48]. Semiconductor-metal transition is predicted at $\epsilon_{\text{arm}} = -12\%$ and $\epsilon_{\text{zig}} = -12\%$ or 12%. Under an in-plane compressive strain, the bandgap of bilayer MoSi_2N_4 and WSi_2N_4 is transferred from the indirect to direct state and the bandgap value changes slightly, while the bandgap rapidly decreases with the increasing tensile strain [103].

The vertical (out-of-plane) compressive strain is also demonstrated to effectively tune the electronic properties of bilayer vdW MA_2Z_4 [97]. With the increase of vertical compressive strain, the bandgap of bilayer MoSi_2N_4 monotonically decreases and reaches 0 eV at $\epsilon = 22\%$ (Fig. 8(b)). This is attributed to the opposite energy shift of the states in different layers. This shift is driven by the asymmetric charge redistribution on the inner Z-Z sublayer at the interface. The similar transition is confirmed in other bilayer MA_2Z_4 , and the pressure to realize such a transition ranges from 2.18 to 32.04 GPa.

The potential of 2D materials in industrial-grade low-dimensional nanodevices is further boosted by the enormous design flexibility offered by the vertical vdW heterostructures (vdWHs), in which physical properties can be customized by the vertically stacking of different 2D

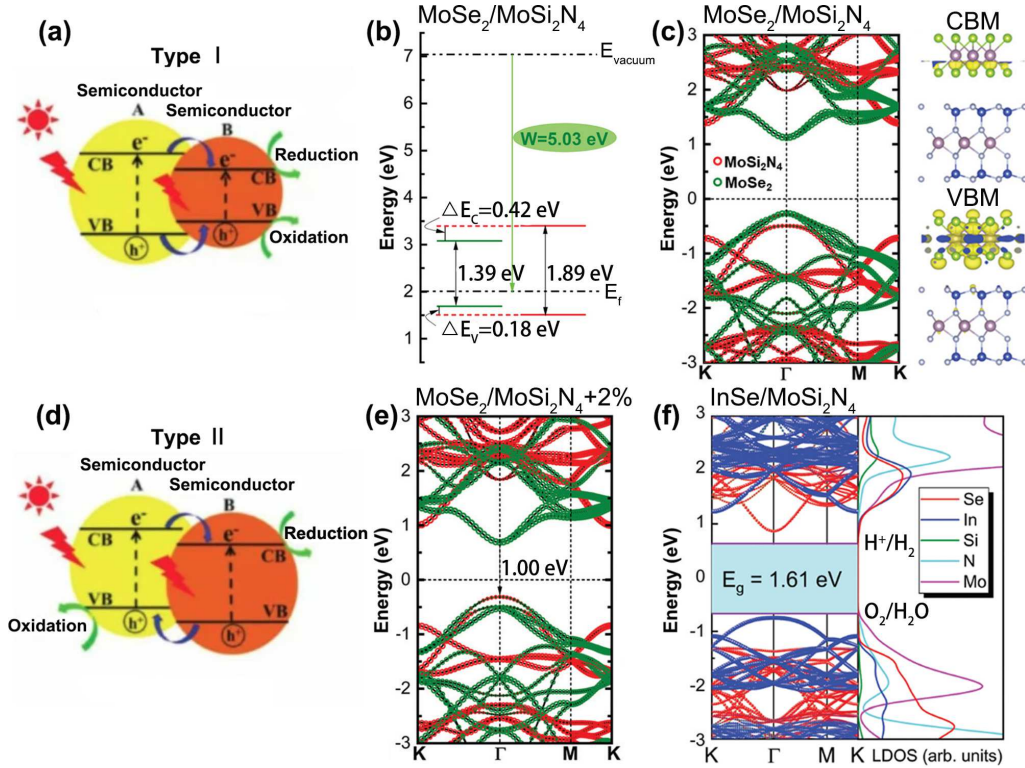


FIG. 9. Semiconducting heterostructures: (a) schematic diagrams of type I (straddling gap) and (d) type II (staggered gap) bands. (b) Type I band alignment of $\text{MoSe}_2/\text{MoSi}_2\text{N}_4$ and (c) charge distribution at CBM and VBM. Type II band structures of (e) $\text{MoSe}_2/\text{MoSi}_2\text{N}_4$ under 2% strain and (f) $\text{InSe}/\text{MoSi}_2\text{N}_4$. [104, 105]

atomic layers. Interlayer coupling of semiconducting vdWHs form 3 types of band alignment: type I (straddling gap binds electrons/holes with the critical ratio of conduction band offset and valence band offset), type II (staggered gap promotes the separation of electrons and holes and suppresses the recombination of electrons and holes), and type III (broken gap). Several previous studies have revealed the electronic properties of vdWHs by stacking 2D semiconductors with MA_2Z_4 .

TMDs/ MA_2Z_4 vdWHs at the ground state belong to the type I alignment, due to the mismatch induced by strain and layer interaction between TMDs and MoSi_2N_4 (Fig. 9) [104, 106]. TMDs provide the main contribution to CBM and VBM. The carrier mobilities of $\text{MoSe}_2/\text{MoSi}_2\text{N}_4$ and $\text{WSe}_2/\text{MoSi}_2\text{N}_4$ are up to $10^4 \text{ cm}^2\text{V}^{-1}\text{s}^{-1}$, which are higher than those of monolayer MoSe_2 and WSe_2 . Under an external electric field or strain, the band structures of TMDs/ MA_2Z_4 vdWHs are transferred from type I to type II. Actually, some other vdWHs by stacking 2D materials (e.g., C_3N_4 , ZnO , InSe and $\text{Cs}_3\text{Bi}_2\text{I}_9$) with MoSi_2N_4 exhibit semiconducting characteristic with type II band structure, indicating promising application in photocatalytic field [105, 107–109]. The carrier mobility of type II $\text{InSe}/\text{MoSi}_2\text{N}_4$ is up to $10^4 \text{ cm}^2\text{V}^{-1}\text{s}^{-1}$, indicating more suitable for photocatalytic nano devices when compared with type I TMDs/ MA_2Z_4 vdWHs. In addition, $\text{BP}/\text{MoSi}_2\text{P}_4$ and

$\text{BP}/\text{MoGe}_2\text{N}_4$ vdWHs possess direct bandgap and belong to type II alignment [110, 111]. Combined with high optical absorption properties, these MA_2Z_4 -based vdWHs would be promising candidates for solar cell devices.

In metal and semiconductor contacts, the Schottky phenomenon with rectification effect in vdWHs occurs. Reducing the Schottky barrier height (SBH) or tuning the Schottky contacts to Ohmic contacts are key challenges for achieving energy efficient and high-performance power devices. MA_2Z_4 -based vdWHs provide opportunities for reconfigurable and tunable nanoelectronic devices. In graphene/ MA_2Z_4 vdWHs, there exists a tiny bandgap [112]. P-type Schottky contacts are formed at the interfaces of two heterojunctions, where the electrons are transferred from graphene to MoSi_2N_4 (WSi_2N_4). The n-type SBH (Φ_n) and the p-type SBH (Φ_p) are 0.922 eV and 0.797 eV, respectively, indicating the presence of a p-type Schottky contact [113]. In contrast, graphene/ MoGe_2N_4 vdWH forms an n-type Schottky contact with a barrier of 0.63 eV [114]. Monolayer Janus MoSiGeN_4 maintains the semiconducting property with an indirect bandgap of 1.436 (2.124) eV obtained by PBE (HSE06) [115]. The vdWHs formed by graphene and Janus MoGeSiN_4 or MoSiGeN_4 have been investigated. The n-type SBH of graphene/ MoGeSiN_4 is 0.63 eV, while the p-type SBH of graphene/ MoSiGeN_4 is 0.74 eV. These SBHs are close to those of MA_2Z_4

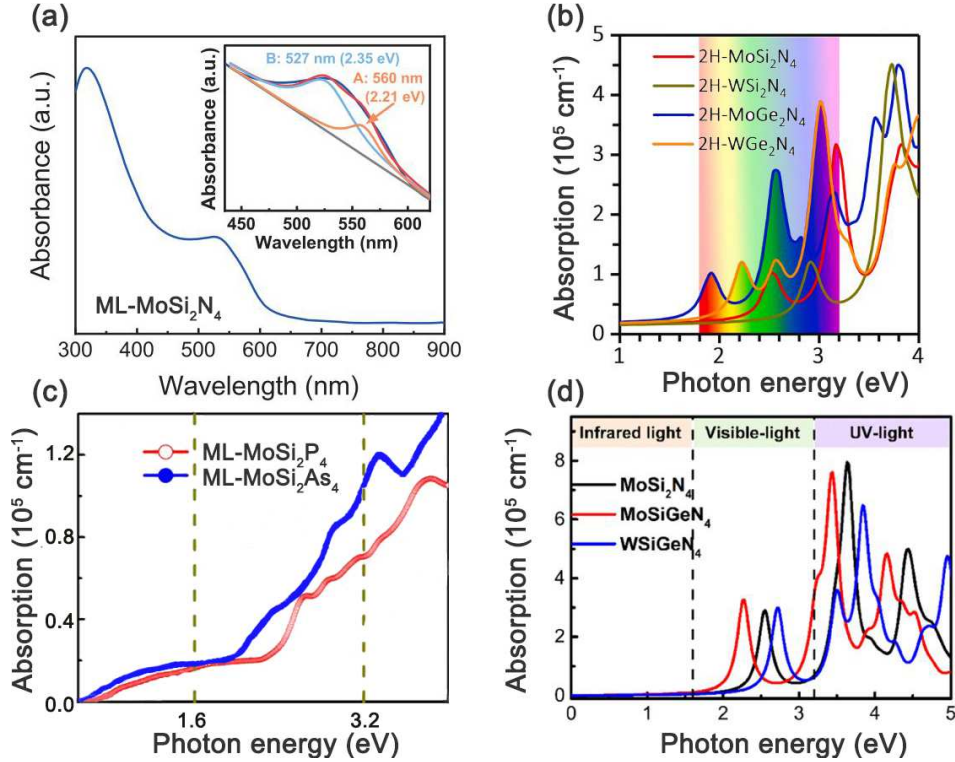


FIG. 10. Optical absorption spectra of monolayer MA_2Z_4 system: (a) $MoSi_2N_4$, (b) MA_2N_4 ($M = Mo/W$, $A = Si/Ge$), (c) $MoSi_2Z_4$ ($Z = P/As$), and (d) Janus $MSiGeN_4$. [28, 47, 72, 102]

($MoSi_2N_4$ and $MoGe_2N_4$), but more adjustable, providing a useful guidance for the design of controllable Schottky nanodevices by using MA_2Z_4 family. Compared with graphene-based vdWHs, the vdWHs formed by MA_2Z_4 and other 2D materials possess better performance in Schottky contact [113, 116]. In $NbS_2/MoSi_2N_4$, Φ_n and Φ_p are 1.642 eV and 0.042 eV, respectively [113]. This ultralow p-type SBH of $NbS_2/MoSi_2N_4$ vdWH suggests the potential of NbS_2 as an efficient 2D electrical contact to $MoSi_2N_4$ with high charge injection efficiency, particularly at room-temperature.

In addition, the Schottky contact types of multilayer vdWHs vary with the order of stacking layers. For instance, the graphene/ $MoSi_2N_4$ / $MoGe_2N_4$ vdWH has an n-type Schottky contact with a SBH of 0.33 eV. While $MoSi_2N_4$ /graphene/ $MoGe_2N_4$ and $MoSi_2N_4$ / $MoGe_2N_4$ /graphene vdWHs are both p-type with a SBH of 0.41 and 0.46 eV, respectively [117]. The contact barriers in the multilayer vdWHs are smaller than those in the bilayer vdWHs, suggesting that the graphene/ $MoSi_2N_4$ / $MoGe_2N_4$ vdWHs provide an effective pathway to reduce the Schottky barrier. This is highly beneficial for improving the charge injection efficiency of contact heterostructures. The p-type Schottky contacts of $MoSi_2N_4$ /graphene or WSi_2N_4 /graphene at the interface can be transferred to n-type by a compressive strain. When a compressive strain of 10% is applied, the transition from Schottky to Ohmic contacts occurs in $MoSi_2N_4$ /graphene and WSi_2N_4 /graphene. However,

no transition is induced by a tensile strain [112, 114].

F. Optical properties

The optical absorption of monolayer MA_2Z_4 system is up to 10^5 cm^{-1} in the visible range [28, 57, 121, 122], which is comparable with that of graphene, phosphorene and MoS_2 . In monolayer $MoSi_2N_4$ (Fig. 10(a)), the experimental results show that a strong peak of optical absorption appears at about 320 nm and a broad peak in the range of 500–600 nm [28]. The calculated results are in good agreement with the experimental data.

Different atomic compositions bring the tunable optical properties to this system [47, 72, 102, 123]. The obvious redshift phenomena of optical absorption spectra are triggered by heavy atoms in M-site MA_2N_4 (Fig. 10(b)), while the absorption coefficient is insensitive to the M-site counterparts. The absorption of $MoSi_2N_4$ and WSi_2N_4 is both 10^5 cm^{-1} in the visible region. The similar red-shift of absorption spectra exhibits in A- or Z-site MoA_2Z_4 as well (Fig. 10(c)). The absorption coefficient, however, is improved with the increasing mass of A or Z atoms. For instance, the absorptions of $MoSi_2Z_4$ ($Z = N/P/As$) are in the order of $MoSi_2N_4 < MoSi_2P_4 < MoSi_2As_4$. In Janus MA_2Z_4 (Fig. 10(d)), the redshift of absorption spectra and the absorption enhancement exist in the lighter $MoSiGeN_4$, compared with $WSiGeN_4$. As for MA_2Z_4 -derived materi-

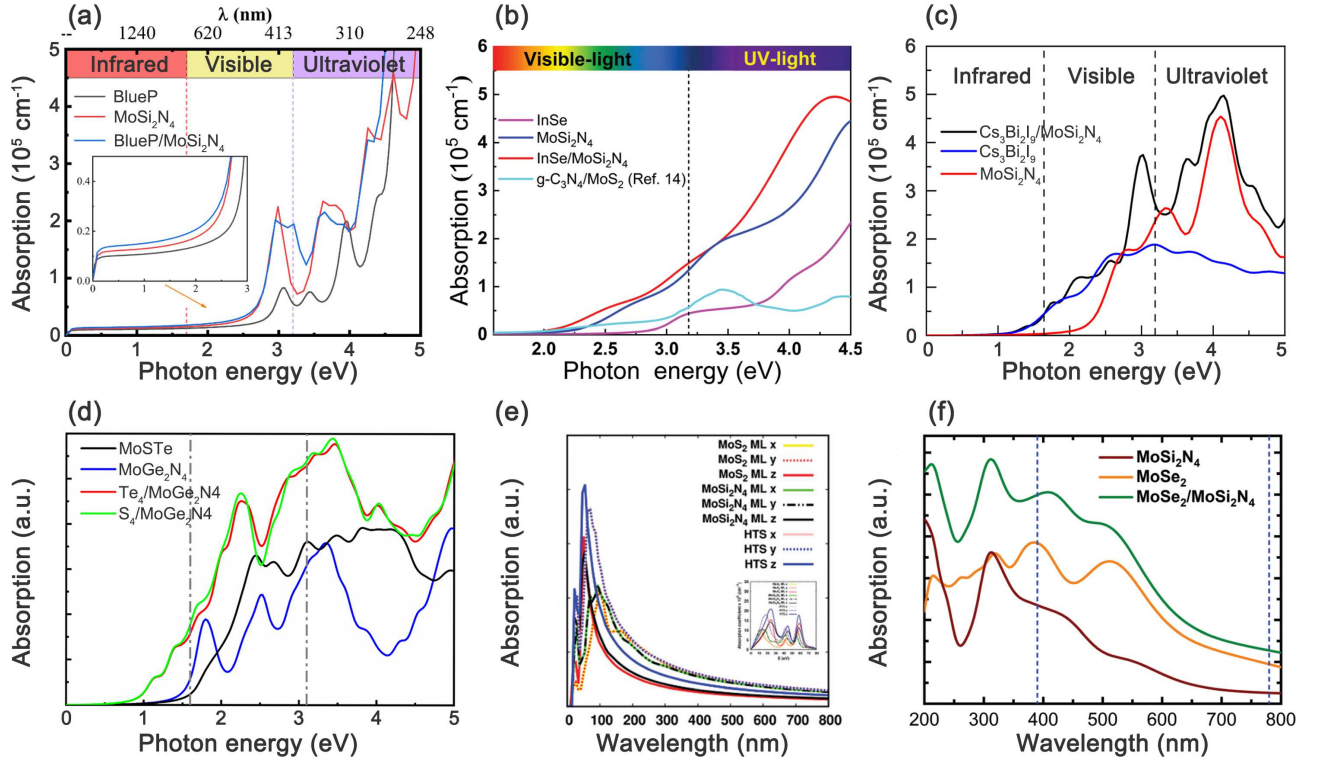


FIG. 11. Optical absorption spectra of MA_2Z_4 based heterostructures: (a) BlueP/ $MoSi_2N_4$ (b) InSe/ $MoSi_2N_4$, (c) $Cs_3Bi_2I_9/MoSi_2N_4$, (d) Janus MoSTe/ $MoGe_2N_4$, (e) $MoS_2/MoSi_2N_4$, and (f) $MoSe_2/MoSi_2N_4$. [104, 105, 109, 118–120]

als (e.g., CrC_2N_4 [60], $SnGe_2N_4$ [62] and $XMoSi_2N_4$ [63]), the absorption of visible light can be up to 10^5 cm^{-1} as well. When Cr is replaced by Mo or W in CrC_2N_4 , the first absorption peak appears in ultraviolet spectra and high frequencies.

Furthermore, optical properties of MA_2Z_4 are shown to be manipulated by strain, surface functionalization, and heterostructure. Firstly, the optical absorption spectrum of $MoSi_2N_4$ shows redshift (blueshift) under a tensile (compressive) strain [96, 124, 125]. The absorption edges decrease with the increasing tensile strain. A 4–10% tensile strain enhances the optical absorption capacity in the visible region up to 43–70%. The reflectance ability (average reflectance rate), meanwhile, is improved from 16% to 23% with the tensile strain from 0% to 10%. Yang et al. [125] found monolayer $MoSi_2N_4$ exhibits more outstanding optical absorption capacity in the ultraviolet range than that in the visible range, especially under biaxial compressive strain. The optical bandgap is evaluated by the slope of absorption peak, in which the corresponding value is 2.47 eV without strain, 2.9 eV with -3% strain and 3.05 eV with -4% strain. Furthermore, compared with monolayer MA_2Z_4 , the bilayer or multilayer MA_2Z_4 shows strong optical absorbance and broad absorption areas as well [102, 126, 127]. When the vertical (out-of-plane) compressive strain increases from 0 to 12%, there exists strong blueshift but only slight decrease of absorption and reflectivity. This manifests that MA_2Z_4 possesses stable optical absorption capacity inde-

pendent of vertical strain and the number of layers, which will be more convenient for experimental fabrication of 2D optoelectronic devices [127].

Secondly, it has been reported that surface functionalization plays an active role in regulating the optical properties of $MoSi_2N_4$, where the adatoms can be Au, F, and Alkali elements (Li, Na, K) [128–130]. In Au- $MoSi_2N_4$, the optical absorption capacity is significantly improved with the increment of Au concentration (6.25–56.3%/unit cell). It can be increased by 1–2 times in the visible light region and by 52% in the ultraviolet region. The results show that Au absorption is beneficial for the photocatalytic activity, making Au- $MoSi_2N_4$ a potential candidate for photoelectrochemical applications and short-wavelength optoelectronic devices. Alkali-metal adsorption not only enhances the optical absorption coefficient but enlarges the absorption area [129]. The absorption coefficient at a wavelength of 380 nm is $0.34 \times 10^5 \text{ cm}^{-1}$ for pristine $MoSi_2N_4$, $0.57 \times 10^5 \text{ cm}^{-1}$ for Li- $MoSi_2N_4$, $1.09 \times 10^5 \text{ cm}^{-1}$ for Na- $MoSi_2N_4$, and $0.89 \times 10^5 \text{ cm}^{-1}$ for K- $MoSi_2N_4$. The light at wavelength of 780 nm is almost unabsorbable by pristine $MoSi_2N_4$. However, the absorption at this wavelength is $0.92 \times 10^5 \text{ cm}^{-1}$ for Li- $MoSi_2N_4$, $1.34 \times 10^5 \text{ cm}^{-1}$ for Na- $MoSi_2N_4$, and $1.14 \times 10^5 \text{ cm}^{-1}$ for K- $MoSi_2N_4$. Na- $MoSi_2N_4$ exhibits the strongest optical response among these three alkali-metal-decorated $MoSi_2N_4$.

Thirdly, in Fig 11, the optical absorption capacity of monolayer $MoSi_2N_4$ is comparable with that of

monolayer MoS₂ and MoSe₂, and better than that of other monolayer 2D materials, such as BlueP, InSe and Cs₃Bi₂I₉. It is interesting that MA₂Z₄-based vdWHs have more excellent optical response than the monolayer MA₂Z₄ and other monolayer 2D materials [104, 105, 109, 111, 118–120, 131]. These enhancements mainly appear in the visible and ultraviolet light range. The high performance of BlueP/MoSi₂N₄ vdWH is in the visible light range of 460–780 nm (the insert of Fig. 11(a)), which is attributed to the overlap of electronic states between valence bands caused by the interlayer coupling and charge transfer [118]. InSe/MoSi₂N₄ vdWH shows great improvement of absorption in the ultraviolet range [105]. The absorption of monolayer Cs₃Bi₂I₉ is superior than that of monolayer MoSi₂N₄ in the photon energy range of 1–2.6 eV, while the relationship reverses in the ultraviolet range (high photon energy), as shown in Fig.11(c). Surprisingly, the absorption is enhanced in the whole range by constructing the Cs₃Bi₂I₉/MoSi₂N₄ vdWH [109]. Similarly, this increasing phenomena appear in Janus MoSTe/MoGe₂N₄, MoS₂/MoSi₂N₄ and MoSe₂/MoSi₂N₄ vdWHs (Fig.11(d–f)) [104, 119, 120], indicating the tunability of optical absorption by forming vdWHs. As for strain effect on the absorption of MA₂Z₄-based heterostructures, the obvious redshift (blueshift) of optical spectrum appears under a tensile (compressive) strain. In BlueP/MoSi₂N₄ vdWH, it is found that a compressive strain restrains the absorption on coefficient in the visible region, while a tensile strain (0–8%) promotes the optical absorption ability [118]. In Janus MoSTe/MoGe₂N₄ vdWH, a compressive strain increases the absorption coefficient in the visible and ultraviolet regions, while a tensile strain enhances it in the infrared region, regardless of which side (S or Te atoms) approaching to MoSi₂N₄ [120].

G. Magnetic properties

It has been reported that group-VB (V/Nb/Ta) MA₂Z₄ nanosheets exhibit robust intrinsic magnetism, and group-VIB (Cr/Mo/W) MA₂Z₄ ones show antiferromagnetic ground states [29, 132–134]. In Table II, NbSi₂N₄, NbSi₂As₄, NbGe₂Z₄, NbGe₂P₄, TaSi₂N₄ and TaGe₂P₄ are ferromagnetic metals with the magnetic moment from 0.37 to 0.78 μ_B per metal atom, while VA₂Z₄ (except VGe₂N₄) are ferromagnetic semiconductors with a magnetic moment of 1 μ_B per V atom. On the other hand, NbSi₂P₄, TaSi₂P₄, TaSi₂As₄, TaGe₂N₄ and group-VIB MA₂Z₄ (e.g., CrSi₂N₄, CrSi₂P₄, CrGe₂N₄, CrGe₂As₄, MoGe₂As₄, WGe₂As₄ and WGe₂P₄) are antiferromagnetic.

For ferromagnetic semiconductors, there exist three types: type-I spin gapless semiconductors (SGSs) (a zero bandgap in one spin channel but a bandgap in another spin channel), type-II SGSs (bandgaps of spin-up or spin-down channel but zero gap for the valence band and conduction band in opposite spin channels), and bipo-

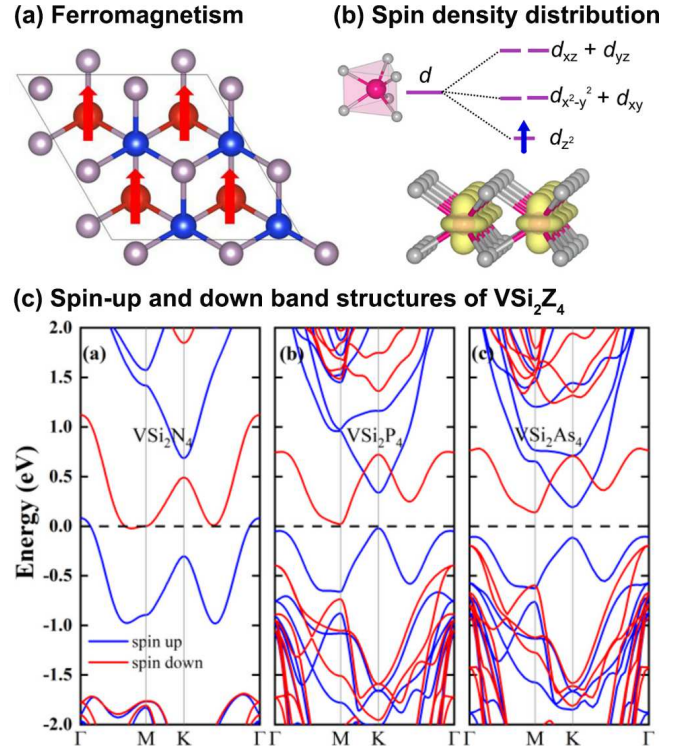


FIG. 12. (a) Magnetic ground states of monolayer VSi₂Z₄. (b) Spin density distribution. (c) Spin-up (blue) and spin-down (red) band structures of VSi₂Z₄ by PBE functional. [135, 136]

lar magnetic semiconductors (BMSs) (the valence band and conduction band in opposite spin channels approaching to Fermi level). 2D SGSs and BMSs with high Curie temperatures are highly desirable for advanced spintronic applications due to their unique electronic structure and high spin polarization [137, 138]. The intrinsic magnetic mechanisms of monolayer MA₂Z₄ nanosheets (e.g., VSi₂N₄, VSi₂P₄ and NbSi₂N₄) have been investigated by dissecting the spin-up and spin-down band structures, magnetic anisotropic energy (MAE) and Curie temperature (T_C).

The magnetic ground states of monolayer VSi₂Z₄ are ferromagnetic (FM) by considering the spin polarization, as shown in Fig. 12(a) [135]. Based on GGA-PBE functional calculations, for the spin-up channel of monolayer VSi₂P₄ both VBM and CBM are located at K point and a direct bandgap of 0.36 eV presents, while VBM at Γ point and CBM at M point indicate an indirect bandgap of 0.42 eV for the spin-down channel (Fig 12(c)). The zero indirect bandgap between spin-up VBM and spin-down CBM implies that monolayer VSi₂P₄ and VSi₂N₄ are type-II SGSs via PBE calculations. In VSi₂As₄, the VBM and CBM for spin channels nearby the Fermi level are in the opposite direction, indicating that the spin-polarized currents would be easily generated with tunable spin polarization by applying a small gate voltage. The results show that the intrinsic ferromagnetism is attributed to the unpaired electron from the metal atom.

TABLE II. Structural properties of magnetic MA_2Z_4 : lattice constants (a), magnetic moment (Mag^{PBE} for PBE and Mag^{HSE} for HSE), magnetic type (FM for ferromagnetic and AFM for antiferromagnetic), magnetic anisotropic energy (MAE), Curie temperature (T_C) with PBE, PBE+ U and HSE. [28, 29, 98]

Struc.	Phase	a (Å)	Mag^{PBE} (μ_B)	Mag^{HSE} (μ_B)	Mag^{HSE} (μ_B)	Type	MAE (μeV)	T_C^{PBE} (K)	$T_C^{\text{PBE}+U}$ (K)	T_C^{HSE} (K)
VSi_2N_4	α_1	2.88	0.97	1.05	1.00–1.19	FM	75.0–76.4	230	350	506–687
VSi_2P_4	α_1	2.88	0.96	1.04	1.00	FM	68.5	230	350	506–687
	δ_4	3.48	1.00	*	1.00	FM	*	235	452	*
VSi_2As_4	α_2	3.72	1.00	*	1.00	FM	*	250	*	*
VGe_2P_4	α_2	3.56	1.00	*	1.00	FM	*	*	*	*
VGe_2As_4	α_2	3.72	1.00	*	1.00	FM	*	*	*	*
NbSi_2N_4	α_1	2.96	0.32–0.57	*	1.00	FM	95.5	*	*	*
NbSi_2P_4	α_1	3.53	*	*	*	AFM	*	*	*	*
NbGe_2N_4	α_1	3.09	0.72	*	1.00	FM	*	*	*	197
TaSi_2P_4	α_1	3.54	*	*	*	AFM	*	*	*	*
TaSi_2As_4	α_2	3.68	*	*	*	AFM	*	*	*	*
TaGe_2N_4	α_1	3.08	0.49	*	1.00	FM	*	*	*	*
YSi_2N_4	α_1	3.07	1.00	*	1.00	FM	*	*	*	90
YSi_2N_4	β_2	3.08	1.00	*	1.00	FM	*	*	*	85

It can be noticed that in VSi_2Z_4 (Fig 12(b)), the d orbital electrons from transition metal occupy the bands approaching to the Fermi level, accompanying with the mixed orbital (e.g., $d_{z^2} + d_{x^2+y^2}$) or transition of orbital composition (e.g., the transition between d_{z^2} and $d_{x^2+y^2}$) [121, 136, 139].

The increment of bandgap is 0.3 eV under the consideration of Coulomb interaction (U) effect [29, 140]. The bandgap of VSi_2Z_4 by HSE functional is larger than that by PBE and PBE+ U . For instances, by HSE functional, VSi_2N_4 possesses a direct bandgap of 0.78 eV at K point, VSi_2P_4 has an indirect bandgap of 0.84 eV with spin-up CBM at Γ point and spin-down VBM at M point, and NbSi_2P_4 exhibits an indirect bandgap of 0.54 eV with spin-up VBM at Γ point and spin-down CBM at M point. The comparison with the three calculation method shows that the bandgap increases from PBE, PBE+ U to HSE. However, the spin polarizations under these methods are still high since there exists only one spin channels around the Fermi level.

Magnetic anisotropic energy (MAE) of NbSi_2N_4 , VSi_2N_4 and VSi_2P_4 are summarized in Table 2. The positive values indicate the in-plane alignment of magnetic moments. Therefore, these ferromagnetic monolayer MA_2Z_4 nanosheets have easy magnetization plane, i.e., none energy consumes when magnetization rotates in the plane. In the finite energy resolution (1 eV), it is found that the total energy has no dependence on the angle of the magnetic moment within the plane, implying the weak in-plane anisotropy of MAE [140], simi-

lar to the recently reported 2D MnPS_3 [141]. MAE of VSi_2Z_4 ($Z = \text{N/P}$) in the range of 0.11 to 0.25 meV per magnetic atom is lower than other 2D materials (e.g., 0.8 meV of CrI_3 [142], 0.72 meV of Fe_3P [143] and 1 meV of Fe_3GeTe_2 [144]), and close to CrCl_3 (0.02 meV), CrBr_3 (0.16 meV), NiI_2 [145] (0.11 meV) and FeCl_2 [146] (0.07 meV).

Curie temperature (T_C) of VSi_2N_4 , VSi_2P_4 and VSi_2As_4 is 230, 235, and 250 K, respectively. [135], which is much higher than 45 K for monolayer CrI_3 [147] and 130 K for monolayer Fe_3GeTe_2 [148]. In Akanda's paper [140], the normalized magnetization of VSi_2N_4 and VSi_2P_4 based on Monte Carlo calculations follows to the analytic expression: $m(T) = (1 - T/T_C)^\beta$, as shown in Fig. 14. The results from PBE+ U show that T_C of VSi_2N_4 and VSi_2P_4 are 350 and 452 K, respectively, which are above room temperature. The difference of predicted T_C is ascribed to the unequal calculation method using different DFT functionals. T_C of VSi_2N_4 by HSE functional is up to 506–687 K. T_C of Janus VSiGeN_4 and VSiSnN_4 is 507 K and 347 K, respectively [136]. With the same functional (e.g., PBE+ U), the transition temperature of monolayer MA_2Z_4 is higher than that of other 2D magnets (e.g., TcGeSe_3 , TcGeTe_3 , ScCl , YCl , LaCl , LaBr_2 , CrSBr , etc.) with high T_C over room temperature [149, 150].

The magnetic properties of MA_2Z_4 family can be tuned by strain, adatoms and defects [136, 139, 140, 151–153]. Similar to the case of magnetic thin films [154–156], strain or stress also has a significant effect on magnetic

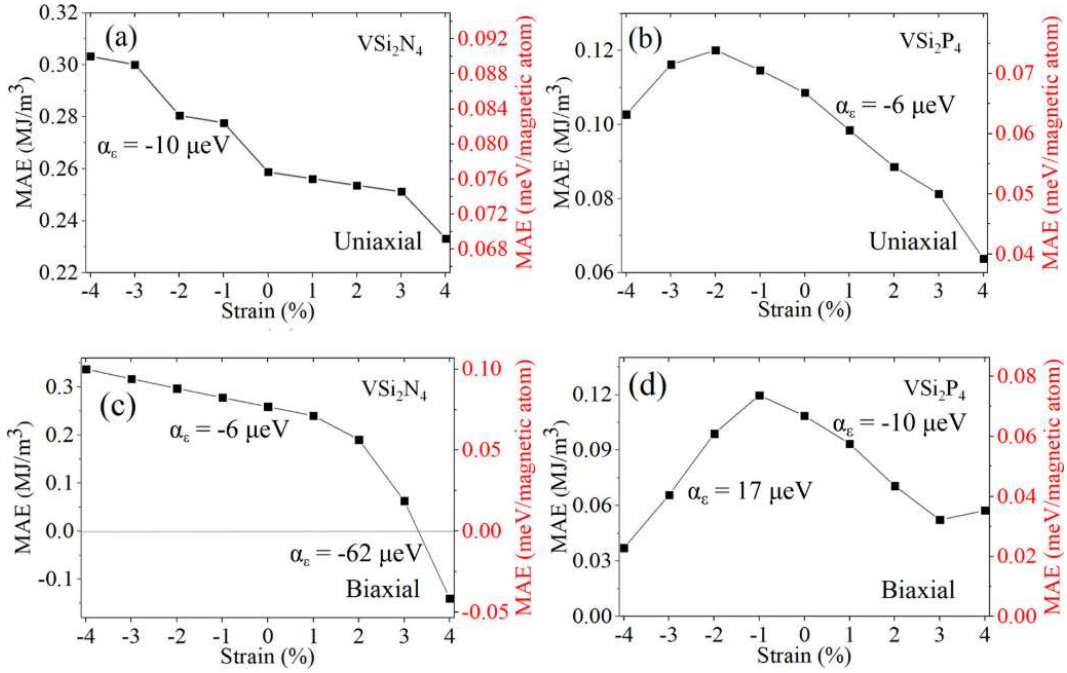


FIG. 13. Strain effect on MAE calculated with PBE(SOC) + U : (a) VSi_2N_4 and (b) VSi_2P_4 under a uniaxial strain, (c) VSi_2N_4 and (d) VSi_2P_4 under a biaxial strain. [140]

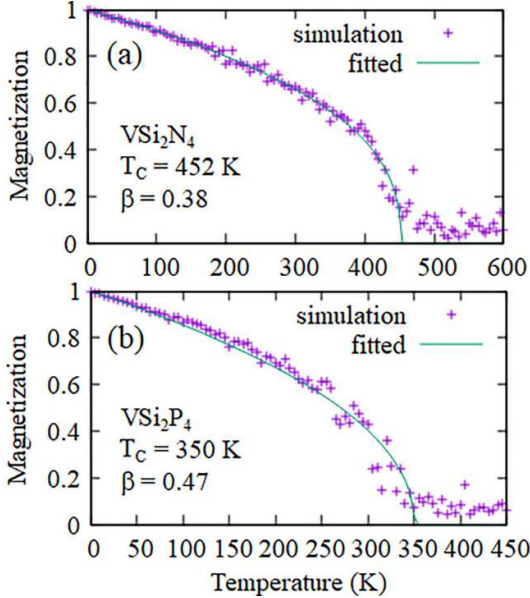


FIG. 14. Monte Carlo calculations of the normalized magnetization as a function of temperature for (a) VSi_2N_4 and (b) VSi_2P_4 . The solid lines show the best fits to the analytical expression. [140]

behaviors of monolayer MA_2Z_4 . The strain coefficient (α_ϵ) is defined as the sensitivity of MAE to strain, which is expressed as $\alpha_\epsilon = dE_{\text{MAE}}/d\epsilon$. In VSi_2N_4 , α_ϵ is $-10 \mu\text{eV}/\%$ under a compressive uniaxial strain and $-6 \mu\text{eV}/\%$ under a biaxial strain, while in VSi_2P_4 , $\alpha_\epsilon = -$

$6 \mu\text{eV}/\%$ under a tensile uniaxial strain, $-10 \mu\text{eV}/\%$ under a tensile biaxial strain, and $17 \mu\text{eV}/\%$ under a compressive biaxial strain (Fig. 13). The strain sensitivity of both two materials is lower than that of CrSb ($32 \mu\text{eV}/\%$) [157]. When the biaxial strain is up to 3–4%, the spin direction of VSi_2N_4 rotates from in-plane to out-of-plane state [139, 140].

Additionally, substitutional doping and atomic vacancies induce the transition of nonmagnetic state in MoSi_2N_4 to magnetic state. Transition metal substitutional doping (e.g., Ag, Au, Bi, Fe, Mn, Pb and V) induces the asymmetric spin channels in MoSi_2N_4 with generating a magnetic moment of $1.00\text{--}5.87 \mu_B$ [153, 159]. Schwingenschlöggl et al. [152] reported that N-site vacancy in MoSi_2N_4 leads to the spin-majority bands crossing the Fermi level. N- and Si-site vacancies generate a magnetic moment of 1.0 and $2.0 \mu_B$, respectively. The nonmagnetic state in MA_2Z_4 -derived $\text{MoN}_2\text{X}_2\text{Y}_2$ ($\text{XY} = \text{AlO}, \text{GaO}, \text{InO}$) nanosheets is transferred to ferromagnetic state by a hole doping [134]. Li et al. [160] found the element substitution of nitrogen by carbon causes different magnetic moments in monolayer $\text{MSi}_2\text{C}_x\text{N}_{4-x}$ ($M = \text{Cr}/\text{Mo}/\text{W}$, $x = 1$ or 2). The position of carbon atoms determines the ground state of magnetic moments. Monolayer CrSi_2CN_3 (C bridged Si and Mo) is predicted as ferromagnetic half-metal, where the magnetic moments is mainly originated from Cr atoms ($0.72 \mu_B$ per atom). There exist three AFM structures, i.e., $\text{CrSi}_2\text{N}_2\text{C}_2$ (two C atoms located at two outermost sites), $\text{MoSi}_2\text{N}_2\text{C}_2$ and $\text{CrSi}_2\text{N}_3\text{C}$ (one C atoms located at outermost site). The magnetic moments are ascribed to the C and metal atoms. The FM

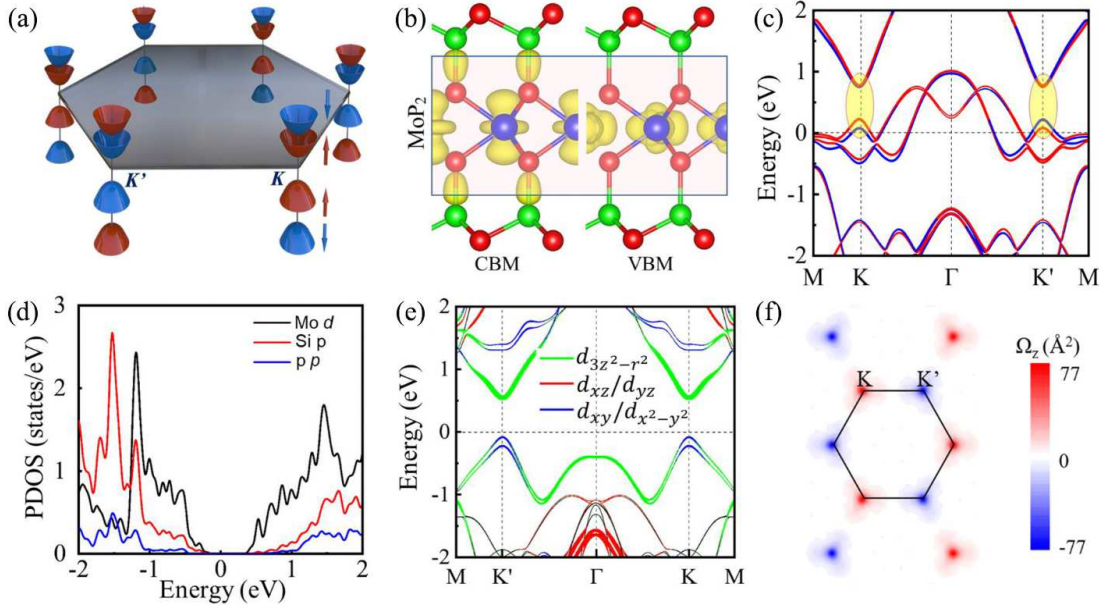


FIG. 15. (a) Schematic of the valleys near the K and K' points. (b) Charge densities at the VBM and CBM of MoSi_2P_4 . (c) Band structure of MoP_2 . (d) Partial densities of states (PDOSs) of MoSi_2P_4 . (e) Orbital-projected band structure of MoSi_2P_4 . (f) Berry curvature of MoSi_2P_4 with nonzero Berry curvature indicating the abnormal transverse velocity. [158]

states in half-metallic 2D systems are attributed to the hole-mediated double exchange, while the AFM states are originated from the super-exchange.

MA_2Z_4 family also has spin-valley properties. As an emerging degree of freedom, valley refers to the presence of multiple energy extremal points in the Brillouin zone (BZ) for low-energy carriers in a semiconductor. Analogous to charge and spin, the valley degree of freedom can be exploited for information encoding and processing, leading to the concept of valleytronics [161]. The spin-valley feature of semiconductors in MA_2Z_4 family has been systematically studied. Taking into account the spin-orbit coupling (SOC), valley spin splittings of MA_2Z_4 appear near both the CBM and VBM. The remarkable splitting near VBM is 139–500 meV, but the spin splitting near CBM is tiny [158, 162–164].

Six kinds of monolayer MA_2Z_4 ($M = \text{Mo}/\text{W}$, $A = \text{C}/\text{Si}/\text{Ge}$, $Z = \text{N}/\text{P}/\text{Ge}$) nanosheets, i.e., MoSi_2P_4 , MoSi_2As_4 , WSi_2P_4 , WSi_2As_4 , WGe_2P_4 and WGe_2As_4 , possess strong spin-valley coupling [158, 165]. They are all direct bandgap semiconductors with band extrema located at the inequivalent K and K' point (Fig. 15(a)). A remarkable spin splitting near the VBM is shown in all the six monolayers with SOC, and the splitting in W-based compounds is larger than that in Mo-based ones. The spin valleys are attributed to the MZ_2 layer by analysing DOS and charge distribution (Fig. 15(b)). Furthermore, the comparison of spin band structures between monolayer MoP_2 (Fig. 15(c)) and MoSi_2P_4 (Fig. 15(e)) shows that there exist other interfering states in the energy range of the valleys of MoP_2 . This manifests that the AZ layers play the role of structural stabi-

lizer and protect the valley states from the interference of the p orbitals of Z atoms and d orbitals of M atom. Time-reversal symmetry always constrains the valley-polarized current. Nonzero Berry curvature of MA_2Z_4 in Fig. 15(f) indicates the abnormal transverse velocity proportional to the Berry curvature would be generated, leading to a spatial separation of the carriers coupled to two different valleys. The carriers from different valleys are accumulated at opposite sides, resulting in an anomalous valley Hall effect. [158, 166]

Monolayer MoSi_2As_4 is found to exhibit ‘perfect valleys’ with no interference from other part of Brillouin zone, as well as multiple-folded valleys (Fig. 16) [166]. The another valley is originated from the second unoccupied conduction band, which enlarges the degree of freedom in energy. The calculation results show that the electron can be selectively pumped from VBM to CBM with a low photon energy of 0.41 eV. With 1.00 eV energy input, the electron can be excited to the VBM and second unoccupied conduction band, indicating the potential application of MoSi_2As_4 for multiple-information operator and storage in valleytronic devices.

The experimentally synthesized MoSi_2N_4 and WSi_2N_4 are indirect bandgap semiconductors in which CBM is located at K (or K') and VBM at Γ point, limiting their potential utilization in valleytronic devices. Nevertheless, the difference between the uppermost valence band at K and Γ point is small (e.g., 144.4 meV in MoSi_2N_4). Strain engineering could eliminate this small difference. The indirect bandgap of MoSi_2N_4 is transferred to the direct bandgap under a compressive strain of 2% and the direct-gap state maintains until a compressive strain up

to 4% [161, 162]. Monolayer MoSi_2N_4 with -4% strain possesses a large spin splitting and strong spin valley coupling (valleys K and K') and thus would be an ideal valleytronic materials.

For other magnetic members in MA_2Z_4 family, the coupling between magnetism and valley provokes the quantum anomalous Hall (QAH) effect. The spin splitting of VSi_2N_4 is 102.3 meV (27.3 meV) at VBM (CBM) [37]. In contrast, the spin splitting of VSi_2P_4 is 49.4 meV at CBM but can be neglected at VBM [167]. Ma et al. [167] separately considered the effect of SOC or magnetic exchange interaction on spin splitting of VSi_2P_4 , and proposed that the combined effect causes its spontaneous valley polarization (Fig. 17). The spin splitting energy at K and K' points is expressed as $\Delta^{\text{K/K}' } = E_{\uparrow}^{\text{K/K}' } - E_{\downarrow}^{\text{K/K}' }$, \uparrow and \downarrow mean spin-up and spin-down channels. With the magnetic exchange interaction, the broken time-reversal symmetry leads to $\Delta_{\text{mag}}^{\text{K}} = \Delta_{\text{mag}}^{\text{K}'}$; with SOC, the time-reversal symmetry results in $\Delta_{\text{SOC}}^{\text{K}} = -\Delta_{\text{SOC}}^{\text{K}'}$; with the synergistic effect, the net spin splitting should be the $\Delta_{\text{mag}}^{\text{K}} + \Delta_{\text{SOC}}^{\text{K}}$ at K point and $\Delta_{\text{mag}}^{\text{K}'} + \Delta_{\text{SOC}}^{\text{K}'}$ at K' point. Li et al. [168] found Hubbard- U can effectively tune the phase diagram of MA_2Z_4 family, and result in intriguing magnetic, valley and topological features. When $U = 2.25$ and 2.36 eV, the QAH phase and valley struc-

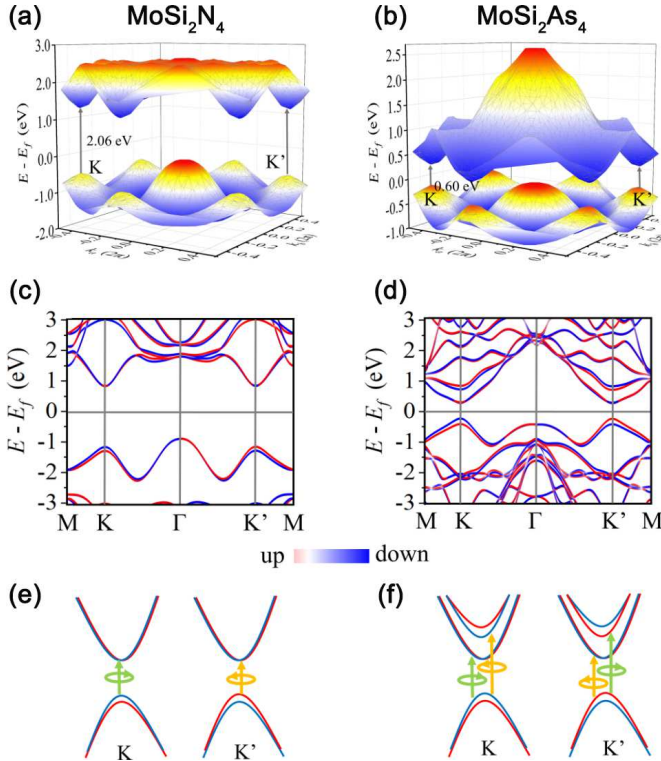


FIG. 16. Spin-valley band structures of monolayer MoSi_2N_4 and MoSi_2As_4 : (a) (b) 3D CBM and VBM of MoSi_2N_4 and MoSi_2As_4 ; (c) (d) spin down and spin up band with SOC. Comparison between (e) traditional valleys and (f) multiple-folded valleys. [166]

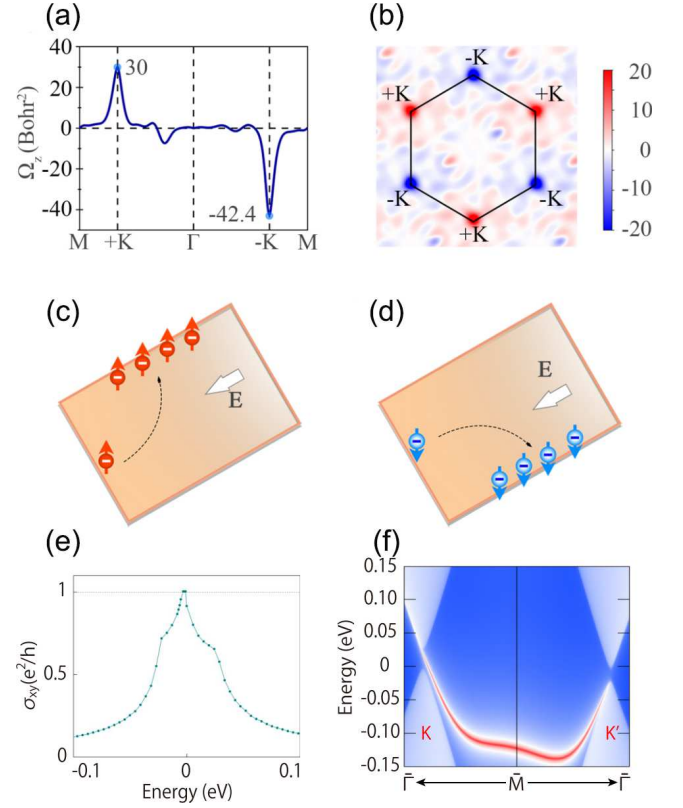


FIG. 17. Berry curvature of monolayer VSi_2P_4 (a) as a curve along the high-symmetry points and (b) as a counter map over the 2D Brillouin zone. (c) (d) Diagrams of the anomalous valley Hall effect under an electron doping and an in-plane electric field, but with opposite magnetization. (e) Anomalous Hall conductivity versus chemical potential with SOC. (f) The corresponding edge spectrum for the QAH state with SOC. Note that the plot is centred at the M point, so the left valley is K and the right valley is K' . [167, 168]

ture coexist, as shown in Fig. 17(e) and (f). Besides, strain effect promotes the trivial topology in VSi_2P_4 and VA_2Z_4 -derived materials ($\text{VN}_2\text{X}_2\text{Y}_2$) [167–169]. There exists an edge state connecting the valence and conduction bands under a compressive strain of 2.1% [167] and a biaxial tensile strain [168]. Recent first-principles calculations reveal 2D MSi_2Z_4 with 1T' structure as large-bandgap and tunable quantum spin Hall insulator, which possesses a protected spin-polarized edge state and a large spin-Hall conductivity [170].

III. PROSPECTIVE APPLICATION

A. Transistors

Semiconductors in 2D MA_2Z_4 family have atomic-scale thickness, ambient stability, suitable bandgap and excellent electronic mobilities, indicating that this family could be promising candidates for the new-generation

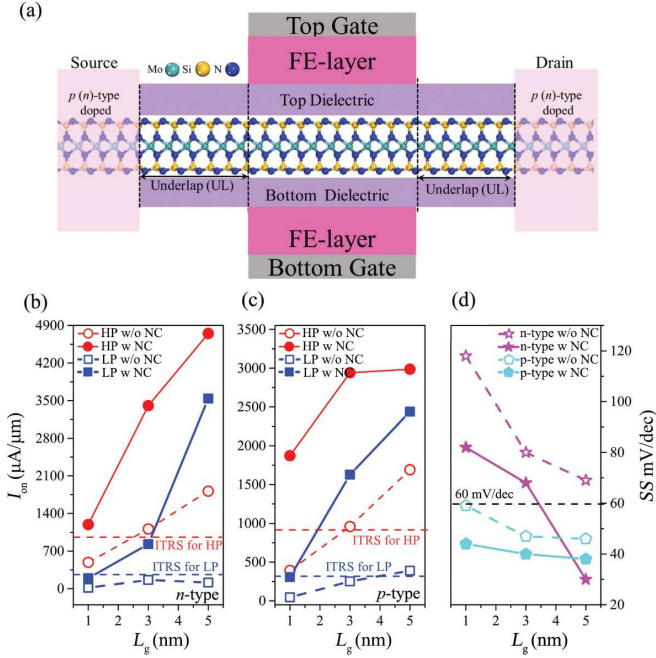


FIG. 18. (a) Nanodevice design of monolayer MA₂Z₄-based transistor. On-current (I_{on}) of (b) n-type and (c) p-type versus gate length (L_g). (d) Subthreshold swing (SS) versus L_g . [171]

miniaturized field-effect transistors (FETs) [171–175]. Double-gate metal-oxide-semiconductor FET (DG MOSFET) based on monolayer MoSi₂N₄ has been designed and investigated [171, 172]. This kind of FET has advantages of high operating frequency, good gain controllability and low feedback capacitance. There are three factors to evaluate the performance of DG MOSFET, i.e., on-current (I_{on}), gate control, and intrinsic delay time and power consumption.

I_{on} represents the device operating speed, while off-current (I_{off}) means the static power dissipation. According to the International Technology Roadmap for Semiconductors (ITRS) published in 2013, the standard of I_{on} (I_{on}/I_{off}) is $900 \mu A/\mu m^{-1}$ (9.0×10^3). The highest I_{on} of n-type (p-type) DG monolayer MoSi₂N₄ MOSFET is up to $1813 \mu A/\mu m^{-1}$ ($1690 \mu A/\mu m^{-1}$), as shown in Fig. 18(b) and (c) [171], which is 70% (80%) higher than n-type (p-type) DG monolayer MoS₂ MOSFET [176]. Subthreshold swing (SS) can reflect the switching rate of MOSFET between the on and off states, which always describes the gate-control ability in the subthreshold region. SS of DG monolayer MA₂Z₄ MOSFET is predicted as 69 mV dec^{-1} for the n-type and 52 mV dec^{-1} for the p-type when the optimum I_{on} is reached. As for sub-5 nm scale MOSFETs, the value of SS should be below the Boltzmann limit at room temperature (60 mV dec^{-1}) since the short channel effect would cause the coexist of tunneling current and thermoionic current, and further influence the overall performance of devices. When gate length (L_g) is below 5 nm, SS of p-type and n-type MA₂Z₄ MOSFETs

is $46\text{--}52 \text{ mV dec}^{-1}$ (Fig. 18(d)) [171, 172]. Switching speed in MOSFETs is described by the intrinsic delay time and power consumption. The ITRS standard of delay time for the high performance and low power is 0.423 and 1.493 ps, respectively. Besides, ITRS requirements of power consumption for the high performance and low power are 0.24 and $0.28 \text{ fJ}\mu m^{-1}$, respectively. DG monolayer MA₂Z₄ MOSFET with an optimum assembly can meet the standards. In brief, the design of device determines whether DG monolayer MA₂Z₄ MOSFET satisfies the ITRS standard in terms of the structural parameters, like gate length, doping concentration to the source and drain, and underlap length between gate and electrodes.

B. Photocatalyst

Photocatalytic process can be described by four important steps: (1) light absorption to generate electron-hole pairs, (2) separation of excited charges to suppress the electron-hole recombination, (3) transfer of electrons and holes to the surface of photocatalysts, and (4) utilization of charges on the surface for redox reactions [177, 178]. The typical reactions are water splitting and CO₂ reduction, which are important for the environment and dual-carbon confinement strategy. 2D MA₂Z₄ systems with high optical absorption could be prospective candidates for photocatalytic applications.

The band edges of photocatalyst candidate in 2D MA₂Z₄ systems must straddle the standard redox potentials. The conduction band edge (CBE) of monolayer MoSi₂N₄ is about 0.71 eV, higher than the H⁺/H₂ reduction level. The valence band edge (VBE) is about 0.19 eV, lower than the O₂/H₂O oxidation level. Band edges of monolayer MoSi₂N₄ straddle the water redox potentials in both highly acidic and neutral conditions (Fig. 19(a)). In contrast, the band edges of monolayer WSi₂N₄ (WGe₂N₄) only satisfy the standard in the highly acidic (neutral) condition [47, 124]. Group-IVB MSi₂N₄ nanosheets with appropriate band edges are considered as the most suitable materials among 2D MA₂Z₄ family for both water splitting and CO₂ reduction application [121]. It is revealed that adatoms reduce the bandgap of MoSi₂N₄ and further promote the possibility of photocatalytic process [128, 129, 179]. The CBE of Au-MoSi₂N₄ is closer to the level for CO₂/HCOOH reduction and thus can easily transfer charges to CO₂ and produce natural gas (HCOOH, HCHO, CO, CH₄, and CH₃OH). The VBE of Au-MoSi₂N₄ approaching to the O₂/H₂O redox potential is beneficial for the interaction between holes and H₂O, and restrains the electron-hole recombination (Fig. 19(b)) [128]. Meanwhile, Li and Na absorption can improve the capacity of water splitting by using MoSi₂N₄ [129]. The adjustable CBE and VBE are observed in MA₂Z₄-based heterostructures (e.g., BlueP/, InSe/ and MoSiGeN₄/MoSi₂N₄) [105, 118, 126, 180–182], providing more possibility of this family for photocatalytic devices.

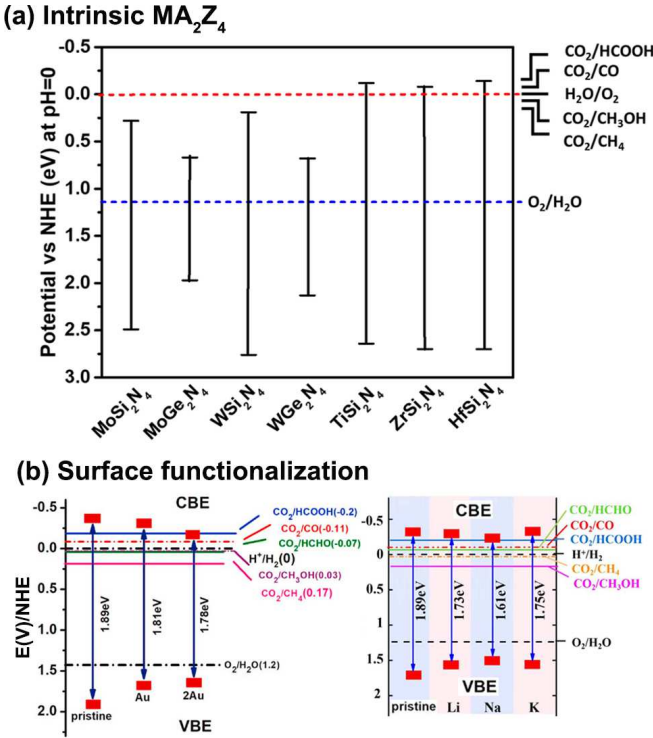


FIG. 19. Band edge positions with respect to water redox and CO_2 reduction levels of (a) monolayer MA_2Z_4 members and (b) MoSi_2N_4 after surface functionalization. The normal hydrogen electrode (NHE) potential is set as 0 eV. [121, 128, 129]

The other important factor of photocatalysis is the absorption of reactive atoms or molecules, which determines the electron transition to the surface and the charge utilization for redox reactions. The optimal site for hydrogen or CO_2 absorption in monolayer MA_2Z_4 is reported as Z site due to the lowest spontaneous binding energy compared with other sites [121, 183]. The Gibbs free energy for the hydrogen adsorption (ΔG_{H^*}) on monolayer MoSi_2N_4 and WSi_2N_4 is calculated to be 2.51 and 2.79 eV, respectively, which is much larger than the ideal value ($\Delta G_{\text{H}^*} = 0$ eV). This indicates the weak binding of hydrogen in pristine monolayer MSi_2N_4 ($\text{M} = \text{Mo}/\text{W}$) and inertial hydrogen evolution reaction (HER) activity [183]. The HER performance of MSi_2N_4 , as well as N_2 reduction reaction (NRR), can be triggered by introducing N-site vacancy [183–186]. As shown in Fig. 20, it is obvious that the vacancy significantly influence ΔG_{H^*} . ΔG_{H^*} is decreased about 2–3 times by M-site vacancy and approaches to zero by N-site vacancy ($\Delta G_{\text{H}^*} = -0.14$ eV in MoSi_2N_4 and -0.02 eV in WSi_2N_4). This manifests that the HER performance of MSi_2N_4 with the outermost N-site vacancy is comparable with and even better than that of Pt. On the other hand, transition metallic atomic doping and strain engineering are verified as the effective strategies to tune ΔG_{H^*} and trigger HER, oxygen evolution reaction (OER) or oxygen reduction reac-

tion (ORR) activity [185, 187, 188]. Particularly, $|\Delta G_{\text{H}^*}|$ is calculated as only 0.05 eV in WSi_2N_4 with Fe-doping at Si-site. A 3% tensile strain results in $\Delta G_{\text{H}^*} = 0.015$ eV in NbGe_2N_4 .

In the MA_2Z_4 family, there exist other good photocatalysts with appropriate ΔG [123, 132, 189, 190], for examples TiSi_2N_4 , HfA_2Z_4 , ZrA_2Z_4 , Janus MSiGeN_4 , etc. Recently, a theoretical method in multilevel is proposed to screen appropriate candidates for hydrogen evolution in MA_2Z_4 family [189]. There exist four screening criteria: (1) small structural deformation after hydrogen absorption to maintain the potential stability during the HER processes, (2) low absolute value of Gibbs free energy ($|\Delta G| \rightarrow 0$) with hydrogen adsorption, (3) suitable bandgaps, (4) high environmental stability. Taking these factors in mind, the multilevel screening workflow discovers seven MA_2Z_4 with great stability and highly active HER among 144 MA_2Z_4 structures, i.e., α_1 - VGe_2N_4 , α_1 - NbGe_2N_4 , α_1 - TaGe_2N_4 , α_1 - NbSi_2N_4 , α_2 - VGe_2N_4 , α_2 - NbGe_2N_4 , and α_2 - TiGe_2P_4 . Monolayer α_1 - NbSi_2N_4 with the lowest formation energy is considered as the most promising 2D MA_2Z_4 material for the HER application along the synthesis routine. At low H coverage ($\theta < 25\%$), the optimal $|\Delta G|$ of these seven MA_2Z_4 is lower than 0.1 eV, which is comparable with or even superior to that of Pt (-0.09 eV at $\theta = 25\%$). A descriptor (E_{LUS}) is proposed as energy level of the lowest unoccupied state to evaluate the capacity of H adsorption, since hydrogen adsorption is often accompanied with the electron transition to the CBM (for semiconductors) or the Fermi level (for metals). A higher E_{LUS} is prone to restraining electron filling and causing weaker H adsorption. On the contrary, a lower E_{LUS} represents the higher ability of H adsorption. Compared with α_1 - MoSi_2N_4 , α_1 - NbSi_2N_4 with lower E_{LUS} shows higher activity toward HER.

HER performance of monolayer MA_2Z_4 family is also examined by the combination of DFT calculations and machine learning algorithms including support vector regression (SVR), kernel ridge regression (KRR), random forest regression (RFR), extreme gradient boosting regression (XGBR), least absolute shrinkage, and selection operator (LASSO) [190]. ΔG_{H^*} and Gibbs free energy of deuterium (ΔG_{D^*}) can be accurately and rapidly predicted via XGBR by using only simple genetic programming processed elemental features, with a low predictive root-mean-square error of 0.14 eV. ΔG_{H^*} of group-VB MA_2Z_4 is closer to zero, indicating the excellent HER capacity. For example, TaSn_2P_4 (0.07 eV) has a similar absolute value of ΔG_{H^*} as NbSn_2P_4 (-0.05 eV), while ΔG_{H^*} of CrSn_2P_4 (0.23 eV) is nearly 3.5 times higher than that of TaSn_2P_4 (0.07 eV). It can be concluded that M element is the crucial factor for the HER performance of MA_2Z_4 materials. In addition, NbSi_2N_4 with $\Delta G_{\text{H}^*} = -0.041$ eV and $\Delta G_{\text{D}^*} = -0.102$ eV, as well as VSi_2N_4 with $\Delta G_{\text{H}^*} = 0.024$ eV and $\Delta G_{\text{D}^*} = -0.033$ eV is screened as the best HER and deuterium evolution reaction (DER) catalysts among the MA_2Z_4 family.

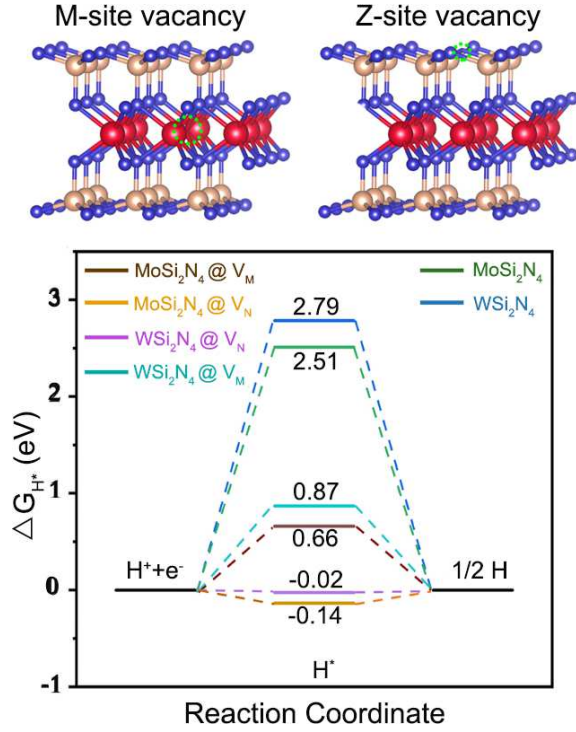


FIG. 20. Crystal structures of monolayer MSi₂N₄ with M- (V_M) and Z-site (V_N) vacancy, and the corresponding Gibbs free energy diagram of HER processing. [183]

As for ORR, the four-electron ($4e^-$) mechanism favors the production of H₂O. The order of ORR activity is MGe₂As₄ > MSi₂As₄ > MSi₂N₄ > MSi₂P₄ > MGe₂P₄ ≈ MGe₂N₄ [191]. Among them, VGe₂As₄, CrGe₂As₄, VSi₂As₄ and NbSi₂As₄ are screened out to be highly promising electrocatalysts with a small overpotential around 0.5–0.6 V. The topmost surface As acts as the active site, and the p-band center of the As atom shows correlation with the adsorption strength of the critical intermediate. Zhang et al. [192] efficiently screened photocatalytic OER catalysts in MA₂Z₄ family via an automated high-throughput workflow. They found the adsorption ability of O atoms determines the catalytic effect. β_2 -ZrSi₂N₄ and β_2 -HfSi₂N₄ are considered as the efficient photocatalytic OER catalysts. In particular, CrGe₂As₄ exhibits outstandingly high ORR activity with ultralow overpotential (0.49 V), which is comparable with the Pt-based catalysts. The metallic conductivity, as well as the moderate adsorption and orbital hybridization between As and O* intermediate, is responsible for the exceptional activity [191].

C. Batteries

Metal-air batteries have great advantages of high-energy-density metal anodes, active air cathodes, light weight, and simple structure, which are convenient to utilize in portable equipments. Bilayer or multilayer vdW

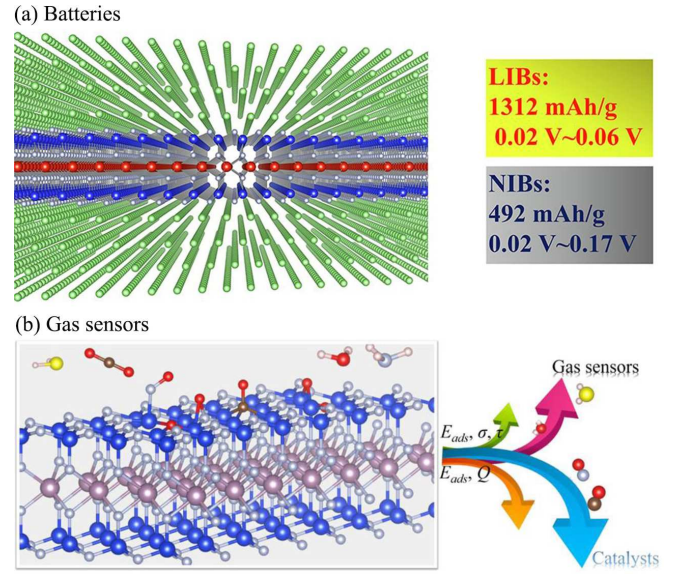


FIG. 21. Diagram of monolayer MA₂Z₄ family in applications of (a) Li-Na batteries and (b) gas sensors. [45, 193]

MoSi₂N₄ shows great potential application as electrodes (both anode and cathode) of Zn-air batteries [194]. On the anode side, the maximum theoretical capacity of Zn in MoSi₂N₄ is up to 257 mAh/g. While on the cathode side, O₂ reduction reaction on the MoSi₂N₄ surface is more efficient than the general sluggish four-electron aqueous O₂ redox reactions. Furthermore, VSi₂N₄ provides two critical specifications (high specific capacity and full battery open-circuit voltage) for the high-performance secondary Li-ion or Na-ion batteries (LIBs/NIBs) (Fig. 21(a)) [193]. The ionic capacity is up to 1312 mAh/g for Li and 492 mAh/g and Na, while the average open-circuit voltages are 0.02–0.06 V for LIBs, and 0.02–0.17 V for NIBs.

D. Sensors

Environmental dependence of physical properties of 2D materials promotes the development of potential applications, e.g., sensors [195–199]. Gas sensor is one of the significant device for detecting gas molecules, especially contaminated and poisonous ones, which can be utilized in the field of industrial harm evaluation, cultivation of agricultural products, assessment of medical drugs, etc. The physisorption behaviors of gas molecules of monolayer MoSi₂N₄ by spin-polarized DFT calculations have been investigated [45, 200]. Due to the weak interaction and small charge transfer, the gas molecules are physically adsorbed on the MoSi₂N₄ surface (Fig. 21(b)). The results show that H₂, N₂, CO, CO₂, NO, NO₂, H₂O, H₂S, NH₃ and CH₄ molecules reduce the bandgap of MoSi₂N₄ (from 1.73 eV to 1.50 eV) [200]. While the absorption of O₂, NO₂ and SO₂ molecules obviously influences the electronic properties of MoSi₂N₄ and even induces the

spin polarization with magnetic moments ($1\text{--}2 \mu_B$). The magnitude of magnetic moments is sensitive to the concentration of gas molecules, which increases with the increment of concentration of NO_2 but decreases with the increment of concentration of SO_2 . This indicates that MoSi_2N_4 -based gas sensor has a high application potential for O_2 , NO , NO_2 and SO_2 detection. Furthermore, the introduction of N vacancy into MoSi_2N_4 improves the absorption performance [45], resulting in MoSi_2N_4 with promising prospects in highly sensitive and reusable gas sensors of H_2O and H_2S molecules.

IV. SUMMARY AND OUTLOOK

In summary, the experimental achievements have brought novel 2D monolayer MoSi_2N_4 and WSi_2N_4 , while theoretical predictions have provided much more possibility of the emerging MA_2Z_4 family due to the structural complexity and component diversity. In this review, we have summarized the latest progress of this novel 2D MA_2Z_4 family with a focus on its physical and chemical properties, as well as its promising applications. Different from transition metal carbides, nitrides and dichalcogenides, this family exhibits more affluent and intriguing features, such as excellent mechanical properties, interesting electronic properties (from insulator to semiconductor to metal) related to the number of total valence electrons, wide range of thermal conductivity ($10^1\text{--}10^3 \text{ W m}^{-1}\text{K}^{-1}$), high optical absorption of visible and ultraviolet light, spin-valley effect, etc. Moreover, the properties of MA_2Z_4 family are manipulable by external fields, providing more degrees of freedom to realize some specific applications. Strain engineering is demonstrated to shrink the band structure of MoSi_2N_4 and induce the well-known ‘Mexican hat’, as well as result in an obvious shift in absorption spectra. By the layered strategy, semiconducting MA_2Z_4 -based vdW heterostructures have promising applications in photocatalysts, while metallic ones effectively reduce the Schottky barrier height and are beneficial for the energy efficient and high-performance power devices. Finally, we survey the perspective applications of MA_2Z_4 , from the aspects of transistors, photocatalysts, batteries, and sensors.

The emerging 2D MA_2Z_4 family with versatile properties and applications opens the mind of low-dimensional structural designs and provides the new possibilities and opportunities to the development of 2D materials. As an outlook, there exist considerable spaces to further understand and exploit the emerging MA_2Z_4 family.

- Firstly, the experience of synthesizing 2D MA_2Z_4 could inspire the idea of synthesizing other 2D materials without knowing their bulk counterparts. Experimental attempts following or beyond the synthesis strategy for monolayer MoSi_2N_4 are intriguing for the advent of new

synthetic 2D materials.

- Secondly, since the development of interdisciplinary, the attention to a potential material is no longer limited to some excellent characteristics. The synergistic effect of multiphysics for practical applications should also be the focus. Although the excellent properties of 2D MA_2Z_4 family have been revealed, synergy of multiphysics coupling would be a crucial method to integrate the versatile properties and maximize their advantages, and even emanate more novel sparks.

- Thirdly, most of the current theoretical predictions on 2D MA_2Z_4 family are made by first-principles calculations. It is highly recommended that modeling and simulation methodologies across scales be developed to understand 2D MA_2Z_4 from electronic, atomistic, microstructure, to device level.

- Fourthly, the sandwich structure of 2D MA_2Z_4 enables more degrees of freedom to elaborate properties and functionalities, calling for more extensive efforts. For instance, the engineering of 2D MA_2Z_4 by asymmetric design of its two sides could be further explored to achieve more versatile structures and functionalities, such as ferroelectricity, multiferroics, Janus structures, etc.

- Fifthly, multilayer or MA_2Z_4 -based vdW heterostructures show great potential in nanodevices. The practical application of 2D MA_2Z_4 family requires more reasonable designs and attempts (e.g., assemble and stacking way, interlayer adaptability, in-plane heterostructure, etc.) to ensure the reliable realization of their advantages.

- Last but not least, the successful preparation of semiconducting monolayer MoSi_2N_4 and WSi_2N_4 by CVD provides the appropriate growth method for this family. However, most of the reported structures, properties, functionalities, and applications of 2D MA_2Z_4 are from the theoretical predictions. Continuous experimental efforts are mandatory to verify the existence of other members (e.g., magnetic VSi_2N_4 and VSi_2P_4) as well as the theoretically predicted properties, applications, and devices.

ACKNOWLEDGMENT

The authors acknowledge the support from the National Natural Science Foundation of China (NSFC 11902150, 12272173), 15th Thousand Youth Talents Program of China, the Research Fund of State Key Laboratory of Mechanics and Control of Mechanical Structures (MCMS-I-0419G01 and MCMS-I-0421K01), the Fundamental Research Funds for the Central Universities (1001-XAC21021), and a project Funded by the Priority Academic Program Development of Jiangsu Higher Education Institutions.

- [1] D. Akinwande, C. J. Brennan, J. S. Bunch, P. Egberts, J. R. Felts, H. Gao, R. Huang, J. S. Kim, T. Li, Y. Li, K. M. Liechti, N. Lu, H. S. Park, E. J. Reed, P. Wang, B. I. Yakobson, T. Zhang, Y. W. Zhang, Y. Zhou, and Y. Zhu, A review on mechanics and mechanical properties of 2D materials—Graphene and beyond, *Extreme Mechanics Letters* **13**, 42 (2017).
- [2] C. Lee, X. Wei, J. W. Kysar, and J. Hone, Measurement of the elastic properties and intrinsic strength of monolayer graphene, *Science* **321**, 385 (2008).
- [3] S. Bertolazzi, J. Brivio, and A. Kis, Stretching and breaking of ultrathin MoS₂, *ACS Nano* **5**, 9703 (2011).
- [4] A. A. Balandin, Thermal properties of graphene and nanostructured carbon materials, *Nature Materials* **10**, 569 (2011).
- [5] D. Li, J. Gao, P. Cheng, J. He, Y. Yin, Y. Hu, L. Chen, Y. Cheng, and J. Zhao, 2D boron sheets: Structure, growth, and electronic and thermal transport properties, *Advanced Functional Materials* **30**, 1904349 (2020).
- [6] X. Qian, J. Zhou, and G. Chen, Phonon-engineered extreme thermal conductivity materials, *Nature Materials* **20**, 1188 (2021).
- [7] C. Wang, B. Lian, X. Guo, J. Mao, Z. Zhang, D. Zhang, B. L. Gu, Y. Xu, and W. Duan, Type-II Ising superconductivity in two-dimensional materials with spin-orbit coupling, *Physical Review Letters* **123**, 126402 (2019).
- [8] J. Bekaert, M. Petrov, A. Aperis, P. M. Oppeneer, and M. V. Milošević, Hydrogen-induced high-temperature superconductivity in two-dimensional materials: The example of hydrogenated monolayer MgB₂, *Physical Review Letters* **123**, 077001 (2019).
- [9] W. Li, J. Huang, X. Li, S. Zhao, J. Lu, Z. V. Han, and H. Wang, Recent progresses in two-dimensional Ising superconductivity, *Materials Today Physics* **21**, 100504 (2021).
- [10] X. Liu, Z. Hao, K. Watanabe, T. Taniguchi, B. I. Halperin, and P. Kim, Interlayer fractional quantum Hall effect in a coupled graphene double layer, *Nature Physics* **15**, 893 (2019).
- [11] Q. Shi, E. M. Shih, M. V. Gustafsson, D. A. Rhodes, B. Kim, K. Watanabe, T. Taniguchi, Z. Papić, J. Hone, and C. R. Dean, Odd- and even-denominator fractional quantum Hall states in monolayer WSe₂, *Nature Nanotechnology* **15**, 569 (2020).
- [12] K. S. Novoselov, A. K. Geim, S. V. M. D. Jiang, Y. Zhang, S. V. Dubonos, I. V. Grigorieva, and A. A. Firsov, Electric field effect in atomically thin carbon films, *Science* **306**, 666 (2004).
- [13] G. AK, Graphene: Status and prospects, *Science* **324**, 1530 (2009).
- [14] M. Yi and Z. Shen, A review on mechanical exfoliation for the scalable production of graphene, *Journal of Materials Chemistry A* **3**, 11700 (2015).
- [15] K. S. Novoselov, D. Jiang, F. Schedin, T. J. Booth, V. V. Khotkevich, S. V. Morozov, and A. K. Geim, Two-dimensional atomic crystals, *Proceedings of the National Academy of Sciences of the United States of America* **102**, 1511 (2005).
- [16] A. K. Geim and I. V. Grigorieva, Van der Waals heterostructures, *Nature* **499**, 419 (2013).
- [17] M. M. Otrokov, I. I. Klimovskikh, H. Bentmann, D. Estyunin, A. Zeugner, Z. S. Aliev, S. Gaß, A. U. Wolter, A. V. Koroleva, A. M. Shikin, M. Blanco-Rey, M. Hoffmann, I. P. Rusinov, A. Y. Vyazovskaya, S. V. Ereemeev, Y. M. Koroteev, V. M. Kuznetsov, F. Freyre, J. Sánchez-Barriga, I. R. Amiraslanov, M. B. Babanly, N. T. Mamedov, N. A. Abdullayev, V. N. Zverev, A. Alfonso, V. Kataev, B. Büchner, E. F. Schwier, S. Kumar, A. Kimura, L. Petaccia, G. Di Santo, R. C. Vidal, S. Schatz, K. Kißner, M. Ünzelmann, C. H. Min, S. Moser, T. R. Peixoto, F. Reinert, A. Ernst, P. M. Echenique, A. Isaeva, and E. V. Chulkov, Prediction and observation of an antiferromagnetic topological insulator, *Nature* **576**, 416 (2019).
- [18] R. Dong, T. Zhang, and X. Feng, Interface-assisted synthesis of 2D materials: Trend and challenges, *Chemical Reviews* **118**, 6189 (2018).
- [19] Y. Huang, Y. H. Pan, R. Yang, L. H. Bao, L. Meng, H. L. Luo, Y. Q. Cai, G. D. Liu, W. J. Zhao, Z. Zhou, L. M. Wu, Z. L. Zhu, M. Huang, L. W. Liu, L. Liu, P. Cheng, K. H. Wu, S. B. Tian, C. Z. Gu, Y. G. Shi, Y. F. Guo, Z. G. Cheng, J. P. Hu, L. Zhao, G. H. Yang, E. Sutter, P. Sutter, Y. L. Wang, W. Ji, X. J. Zhou, and H. J. Gao, Universal mechanical exfoliation of large-area 2D crystals, *Nature Communications* **11**, 2453 (2020).
- [20] M. Yi, Z. Shen, W. Zhang, J. Zhu, L. Liu, S. Liang, X. Zhang, and S. Ma, Hydrodynamics-assisted scalable production of boron nitride nanosheets and their application in improving oxygen-atom erosion resistance of polymeric composites, *Nanoscale* **5**, 10660 (2013).
- [21] M. Yi and Z. Shen, Kitchen blender for producing high-quality few-layer graphene, *Carbon* **78**, 622 (2014).
- [22] M. Yi and Z. Shen, Fluid dynamics: An emerging route for the scalable production of graphene in the last five years, *RSC Advances* **6**, 72525 (2016).
- [23] A. J. Mannix, X. F. Zhou, B. Kiraly, J. D. Wood, D. Alducin, B. D. Myers, X. Liu, B. L. Fisher, U. Santiago, J. R. Guest, M. J. Yacamán, A. Ponce, A. R. Oganov, M. C. Hersam, and N. P. Guisinger, Synthesis of borophenes: Anisotropic, two-dimensional boron polymorphs, *Science* **350**, 1513 (2015).
- [24] B. Feng, J. Zhang, Q. Zhong, W. Li, S. Li, H. Li, P. Cheng, S. Meng, L. Chen, and K. Wu, Experimental realization of two-dimensional boron sheets, *Nature Chemistry* **8**, 563 (2016).
- [25] Y. Zhan, Z. Liu, S. Najmaei, P. M. Ajayan, and J. Lou, Large-area vapor-phase growth and characterization of MoS₂ atomic layers on a SiO₂ substrate, *Small* **8**, 966 (2012).
- [26] Y. Zhang, Y. Yao, M. G. Sendeku, L. Yin, X. Zhan, F. Wang, Z. Wang, and J. He, Recent progress in CVD growth of 2D transition metal dichalcogenides and related heterostructures, *Advanced Materials* **31**, 1901694 (2019).
- [27] K. S. Novoselov, A. Mishchenko, A. Carvalho, and A. H. Castro Neto, 2D materials and van der Waals heterostructures, *Science* **353**, 6298 (2016).
- [28] S. H. Lee, Z. Li, L. Wang, J. Zhou, W. Ma, C. Xu, S. Feng, L. Chen, M. L. Chen, D. M. Sun, X. Q. Chen, H. M. Cheng, and W. Ren, Chemical vapor deposition of layered two-dimensional MoSi₂N₄ materials,

- Science* **369**, 670 (2020).
- [29] L. Wang, Y. Shi, M. Liu, A. Zhang, Y. L. Hong, R. Li, Q. Gao, M. Chen, W. Ren, H. M. Cheng, Y. Li, and X. Q. Chen, Intercalated architecture of MA_2Z_4 family layered van der Waals materials with emerging topological, magnetic and superconducting properties, *Nature Communications* **12**, 2361 (2021).
- [30] J. S. Yang, L. Zhao, S. Q. Li, H. Liu, L. Wang, M. Chen, J. Gao, and J. Zhao, Accurate electronic properties and non-linear optical response of two-dimensional MA_2Z_4 , *Nanoscale* **13**, 5479 (2021).
- [31] L. Kang and Z. Lin, Second harmonic generation of MoSi_2N_4 -type layers, *Physical Review B* **103**, 195404 (2021).
- [32] D. Liang, S. Xu, P. Lu, and Y. Cai, Highly tunable and strongly bound exciton in MoSi_2N_4 via strain engineering, *Physical Review B* **105**, 195302 (2022).
- [33] D. Huang, F. Liang, R. Guo, D. Lu, J. Wang, H. Yu, and H. Zhang, MoSi_2N_4 : A 2D regime with strong exciton-phonon coupling, *Advanced Optical Materials* **10**, 2102612 (2022).
- [34] Z. Wang, X. Kuang, G. Yu, P. Zhao, H. Zhong, and S. Yuan, Electronic properties and quasiparticle model of monolayer, *Physical Review B* **104**, 155110 (2021).
- [35] J. Zhao, X. Jin, H. Zeng, C. Yao, and G. Yan, Spin-valley coupling and valley splitting in the $\text{MoSi}_2\text{N}_4/\text{CrCl}_3$ van der Waals heterostructure, *Applied Physics Letters* **119**, 213101 (2021).
- [36] L. Yan, B. T. Wang, X. Huang, Q. Li, K. Xue, J. Zhang, W. Ren, and L. Zhou, Surface passivation induced a significant enhancement of superconductivity in layered two-dimensional MSi_2N_4 ($M = \text{Ta}$ and Nb) materials, *Nanoscale* **13**, 18947 (2021).
- [37] X. Zhou, R. W. Zhang, Z. Zhang, W. Feng, Y. Mokrousov, and Y. Yao, Sign-reversible valley-dependent Berry phase effects in 2D valley-half-semiconductors, *npj Computational Materials* **7**, 160 (2021).
- [38] Y. Wang, D. Legut, X. Liu, Y. Li, C. Li, Y. Sun, R. Zhang, and Q. Zhang, Mott transition and superexchange mechanism in magnetically doped XSi_2N_4 caused by large $3d$ orbital onsite Coulomb interaction, *Physical Review B* **106**, 104421 (2022).
- [39] Z. Cui, Y. Luo, J. Yu, and Y. Xu, Tuning the electronic properties of MoSi_2N_4 by molecular doping: A first principles investigation, *Physica E: Low-Dimensional Systems and Nanostructures* **134**, 114813 (2021).
- [40] W. Zhou, L. Wu, A. Li, B. Zhang, and F. Ouyang, Structural symmetry, spin-orbit coupling, and valley-related properties of monolayer WSi_2N_4 family, *Journal of Physical Chemistry Letters* **12**, 11622 (2021).
- [41] R. Islam, B. Ghosh, C. Autieri, S. Chowdhury, A. Bansil, A. Agarwal, and B. Singh, Tunable spin polarization and electronic structure of bottom-up synthesized MoSi_2N_4 materials, *Physical Review B* **104**, L201112 (2021).
- [42] Q. Wu and L. K. Ang, Giant tunneling magnetoresistance in atomically thin $\text{VSi}_2\text{N}_4/\text{MoSi}_2\text{N}_4/\text{VSi}_2\text{N}_4$ magnetic tunnel junction, *Applied Physics Letters* **120**, 022401 (2022).
- [43] H. Ma, W. Zhao, Q. Zhang, D. Liu, H. Ren, H. Zhu, Y. Chi, F. Ding, and W. Guo, Chemical environment dependent stabilities, electronic properties and diffusions behaviors of intrinsic point defects in novel two-dimensional MoSi_2N_4 monolayer, *Applied Surface Science* **592**, 153214 (2022).
- [44] H. Zhao, G. Yang, Y. Liu, X. Yang, Y. Gu, C. Wei, Z. Xie, Q. Zhang, B. Bian, X. Zhang, X. Huo, and N. Lu, Quantum transport of sub-10 nm monolayer WGe_2N_4 transistors, *ACS Applied Electronic Materials* **3**, 5086 (2021).
- [45] C. Xiao, Z. Ma, R. Sa, Z. Cui, S. Gao, W. Du, X. Sun, and Q. H. Li, Adsorption behavior of environmental gas molecules on pristine and defective MoSi_2N_4 : Possible application as highly sensitive and reusable gas sensors, *ACS Omega* **7**, 8706 (2022).
- [46] Y. Gao, J. Liao, H. Wang, Y. Wu, Y. Li, K. Wang, C. Ma, S. Gong, T. Wang, X. Dong, Z. Jiao, and Y. An, Electronic transport properties and nanodevice designs for monolayer MoSi_2P_4 , *Physical Review Applied* **18**, 034033 (2022).
- [47] B. Mortazavi, B. Javvaji, F. Shojaei, T. Rabczuk, A. V. Shapeev, and X. Zhuang, Exceptional piezoelectricity, high thermal conductivity and stiffness and promising photocatalysis in two-dimensional MoSi_2N_4 family confirmed by first-principles, *Nano Energy* **82**, 105716 (2021).
- [48] X. Liu, H. Zhang, Z. Yang, Z. Zhang, X. Fan, and H. Liu, Structure and electronic properties of MoSi_2P_4 monolayer, *Physics Letters A* **420**, 127751 (2021).
- [49] Y. Yin, M. Yi, and W. Guo, High and anomalous thermal conductivity in monolayer MSi_2Z_4 semiconductors, *ACS Applied Materials & Interfaces* **13**, 45907 (2021).
- [50] G. H. Lee, R. C. Cooper, S. J. An, S. Lee, A. Van Der Zande, N. Petrone, A. G. Hammerberg, C. Lee, B. Crawford, W. Oliver, J. W. Kysar, and J. Hone, High-strength chemical-vapor-deposited graphene and grain boundaries, *Science* **340**, 1074 (2013).
- [51] K. Liu, Q. Yan, M. Chen, W. Fan, Y. Sun, J. Suh, D. Fu, S. Lee, J. Zhou, S. Tongay, J. Ji, J. B. Neaton, and J. Wu, Elastic properties of chemical-vapor-deposited monolayer MoS_2 , WS_2 , and their bilayer heterostructures, *Nano Letters* **14**, 5097 (2014).
- [52] R. Zhang, V. Koutsos, and R. Cheung, Elastic properties of suspended multilayer WSe_2 , *Applied Physics Letters* **108**, 042104 (2016).
- [53] A. Lipatov, H. Lu, M. Alhabeab, B. Anasori, A. Gruverman, Y. Gogotsi, and A. Sinitzkii, Elastic properties of 2D $\text{Ti}_3\text{C}_2\text{T}_x$ MXene monolayers and bilayers, *Science advances* **4**, eaat0491 (2018).
- [54] M. Alhabeab, H. Lu, S. Zhao, M. J. Loes, N. S. Vorobeva, Y. Dall'Agnese, Y. Gao, A. Gruverman, Y. Gogotsi, and A. Sinitzkii, Electrical and elastic properties of individual single-layer $\text{Nb}_4\text{C}_3\text{T}_x$ MXene flakes, *Advanced Electronic Materials* **6**, 1901382 (2020).
- [55] Q. Wei and X. Peng, Superior mechanical flexibility of phosphorene and few-layer black phosphorus, *Applied Physics Letters* **104**, 251915 (2014).
- [56] Q. Li, W. Zhou, X. Wan, and J. Zhou, Strain effects on monolayer MoSi_2N_4 : Ideal strength and failure mechanism, *Physica E: Low-Dimensional Systems and Nanostructures* **131**, 114811 (2021).
- [57] A. Bafekry, M. Faraji, D. M. Hoat, M. Shahrokhi6, M. M. Fadlallah, F. Shojaei, S. A. H. Feghhi, M. Ghergherehchi, and D. Gogova, MoSi_2N_4 single-layer: A novel two-dimensional material with outstanding mechanical, thermal, electronic, optical, and photocatalytic properties,

- Journal of Physics D: Applied Physics* **54**, 155303 (2021).
- [58] C. A. Marianetti and H. G. Yevick, Failure mechanisms of graphene under tension, *Physical Review Letters* **105**, 245502 (2010).
- [59] T. Li, Ideal strength and phonon instability in single-layer MoS₂, *Physical Review B* **85**, 235407 (2012).
- [60] B. Mortazavi, F. Shojaei, B. Javvaji, T. Rabczuk, and X. Zhuang, Outstandingly high thermal conductivity, elastic modulus, carrier mobility and piezoelectricity in two-dimensional semiconducting CrC₂N₄: A first-principles study, *Materials Today Energy* **22**, 100839 (2021).
- [61] M. Tian, C. Wei, J. Zhang, J. Wang, and R. Yang, Electronic, optical, and water solubility properties of two-dimensional layered SnSi₂N₄ from first principles, *Physical Review B* **103**, 195305 (2021).
- [62] V. D. Dat and T. V. Vu, Layered post-transition-metal dichalcogenide SnGe₂N₄ as a promising photoelectric material: A DFT study, *RSC Advances* **12**, 10249 (2022).
- [63] R. T. Sibatov, R. M. Meftakhutdinov, and A. I. Kochaev, Asymmetric XMoSiN₂ (X=S, Se, Te) monolayers as novel promising 2D materials for nanoelectronics and photovoltaics, *Applied Surface Science* **585**, 152465 (2022).
- [64] S. D. Guo, Y. T. Zhu, W. Q. Mu, L. Wang, and X. Q. Chen, Structure effect on intrinsic piezoelectricity in septuple-atomic-layer MSi₂N₄ (M=Mo and W), *Computational Materials Science* **188**, 110223 (2021).
- [65] S. D. Guo, Y. T. Zhu, W. Q. Mu, and W. C. Ren, Intrinsic piezoelectricity in monolayer MSi₂N₄ (M = Mo, W, Cr, Ti, Zr and Hf), *Europhysics Letters* **132**, 57002 (2020).
- [66] K. A. N. Duerloo, M. T. Ong, and E. J. Reed, Intrinsic piezoelectricity in two-dimensional materials, *Journal of Physical Chemistry Letters* **3**, 2871 (2012).
- [67] M. N. Blonsky, H. L. Zhuang, A. K. Singh, and R. G. Hennig, Ab initio prediction of piezoelectricity in two-dimensional materials, *ACS Nano* **9**, 9885 (2015).
- [68] C. Cui, F. Xue, W. J. Hu, and L. J. Li, Two-dimensional materials with piezoelectric and ferroelectric functionalities, *npj 2D Materials and Applications* **2**, 18 (2018).
- [69] C. M. Lueng, H. L. Chan, W. K. Fong, C. Surya, and C. L. Choy, Piezoelectric coefficients of aluminum nitride and gallium nitride, *Materials Research Society Symposium - Proceedings* **572**, 389 (2000).
- [70] S. D. Guo, W. Q. Mu, Y. T. Zhu, and X. Q. Chen, Coexistence of intrinsic piezoelectricity and ferromagnetism induced by small biaxial strain in septuple-atomic-layer VSi₂P₄, *Physical Chemistry Chemical Physics* **22**, 28359 (2020).
- [71] S. D. Guo, W. Q. Mu, Y. T. Zhu, R. Y. Han, and W. C. Ren, Predicted septuple-atomic-layer Janus MSiGeN₄ (M = Mo and W) monolayers with Rashba spin splitting and high electron carrier mobilities, *Journal of Materials Chemistry C* **9**, 2464 (2021).
- [72] X. Guo and S. Guo, Janus MSiGeN₄ (M = Zr and Hf) monolayers derived from centrosymmetric β -MA₂Z₄: A first-principles study, *Journal of Semiconductors* **42**, 122002 (2021).
- [73] S. D. Guo, Y. T. Zhu, W. Q. Mu, and X. Q. Chen, A piezoelectric quantum spin Hall insulator with Rashba spin splitting in Janus monolayer SrAlGaSe₄, *Journal of Materials Chemistry C* **9**, 7465 (2021).
- [74] T. Zhong, Y. Ren, Z. Zhang, J. Gao, and M. Wu, Sliding ferroelectricity in two-dimensional MoA₂N₄ (A = Si or Ge) bilayers: High polarizations and Moiré potentials, *Journal of Materials Chemistry A* **9**, 19659 (2021).
- [75] Z. Fei, W. Zhao, T. A. Palomaki, B. Sun, M. K. Miller, Z. Zhao, J. Yan, X. Xu, and D. H. Cobden, Ferroelectric switching of a two-dimensional metal, *Nature* **560**, 336 (2018).
- [76] L. Li and M. Wu, Binary compound bilayer and multilayer with vertical polarizations: Two-dimensional ferroelectrics, multiferroics, and nanogenerators, *ACS Nano* **11**, 6382 (2017).
- [77] X. Zhuang, B. He, B. Javvaji, and H. S. Park, Intrinsic bending flexoelectric constants in two-dimensional materials, *Physical Review B* **99**, 054105 (2019).
- [78] L. Dong, J. Lou, and V. B. Shenoy, Large in-plane and vertical piezoelectricity in Janus transition metal dichalcogenides, *ACS Nano* **11**, 8242 (2017).
- [79] B. Javvaji, B. He, X. Zhuang, and H. S. Park, High flexoelectric constants in Janus transition-metal dichalcogenides, *Physical Review Materials* **3**, 125402 (2019).
- [80] J. Yu, J. Zhou, X. Wan, and Q. Li, High intrinsic lattice thermal conductivity in monolayer MoSi₂N₄, *New Journal of Physics* **23**, 033005 (2021).
- [81] C. Shen, L. Wang, D. Wei, Y. Zhang, G. Qin, X. Q. Chen, and H. Zhang, Two-dimensional layered MSi₂N₄ (M = Mo, W) as promising thermal management materials: A comparative study, *Physical Chemistry Chemical Physics* **24**, 3086 (2022).
- [82] T. Li, G. Nie, and Q. Sun, Highly sensitive tuning of lattice thermal conductivity of graphene-like borophene by fluorination and chlorination, *Nano Research* **13**, 1171 (2020).
- [83] Y. Cai, J. Lan, G. Zhang, and Y. Zhang, Lattice vibrational modes and phonon thermal conductivity of monolayer MoS₂, *Physical Review B* **89**, 035438 (2014).
- [84] X. Gu and R. Yang, Phonon transport in single-layer transition metal dichalcogenides: A first-principles study, *Applied Physics Letters* **105**, 131903 (2014).
- [85] P. Torres, F. X. Alvarez, Cartoixà X. , and R. Rurali, Thermal conductivity and phonon hydrodynamics in transition metal dichalcogenides from first-principles, *2D Materials* **6**, 035002 (2019).
- [86] P. Liu, T. Bo, J. Xu, W. Yin, J. Zhang, F. Wang, O. Eriksson, and B. T. Wang, First-principles calculations of the ultralow thermal conductivity in two-dimensional group-IV selenides, *Physical Review B* **98**, 235426 (2018).
- [87] Y. Sun, Z. Shuai, and D. Wang, Reducing lattice thermal conductivity of the thermoelectric SnSe monolayer: Role of phonon–electron coupling, *Journal of Physical Chemistry C* **123**, 12001 (2019).
- [88] A. A. Balandin, S. Ghosh, W. Bao, I. Calizo, and C. Lau, Superior thermal conductivity of single-layer graphene, *Nano Letters* **8**, 902 (2008).
- [89] S. Ghosh, I. Calizo, D. Teweldebrhan, E. P. Pokatilov, D. Nika, A. A. Balandin, W. Bao, F. Miao, and C. N. Lau, Extremely high thermal conductivity of graphene: Prospects for thermal management applications in nanoelectronic circuits, *Applied Physics Letters* **92**, 151911 (2008).
- [90] L. Lindsay and D. A. Broido, Enhanced thermal conductivity and isotope effect in single-layer hexagonal boron nitride, *Physical Review B* **84**, 155421 (2011).

- [91] G. A. Slack, Anisotropic thermal conductivity of pyrolytic graphite, *Physical Reviews* **127**, 694 (1962).
- [92] G. A. Slack, Nonmetallic crystals with high thermal conductivity, *Journal of Physics and Chemistry of Solids* **34**, 321 (1973).
- [93] X. S. Guo and S. D. Guo, Tuning transport coefficients of monolayer MoSi_2N_4 with biaxial strain, *Chinese Physics B* **30**, 067102 (2021).
- [94] Y. Huang, X. Zhong, H. Yuan, and H. Chen, Thermoelectric performance of MoSi_2As_4 monolayer, *Europhysics Letters* **137**, 16002 (2022).
- [95] C. Zhang, F. Wei, X. Zhang, W. Chen, C. Chen, J. Hao, and B. Jia, Thermoelectric properties of monolayer MoSi_2N_4 and MoGe_2N_4 with large Seebeck coefficient and high carrier mobility: A first principles study, *Journal of Solid State Chemistry* **315**, 123447 (2022).
- [96] H. Alavi-rad, Strain engineering in optoelectronic properties of MoSi_2N_4 monolayer: Ultrahigh tunability, *Semiconductor Science and Technology* **37**, 065018 (2022).
- [97] H. Zhong, W. Xiong, P. Lv, J. Yu, and S. Yuan, Strain-induced semiconductor to metal transition in MA_2Z_4 bilayers (M= Ti, Cr, Mo; A= Si; Z= N, P), *Physical Review B* **103**, 085124 (2021).
- [98] Y. Ding and Y. Wang, Computational exploration of stable 4d/5d transition-metal MSi_2N_4 (M = Y-Cd and Hf-Hg) nanosheets and their versatile electronic and magnetic properties, *Journal of Physical Chemistry C* **125**, 19580 (2021).
- [99] Y. Wu, Z. Tang, W. Xia, W. Gao, F. Jia, Y. Zhang, W. Zhu, W. Zhang, and P. Zhang, Prediction of protected band edge states and dielectric tunable quasiparticle and excitonic properties of monolayer MoSi_2N_4 , *npj Computational Materials* **8**, 129 (2022).
- [100] Y. Cai, G. Zhang, and Y. W. Zhang, Polarity-reversed robust carrier mobility in monolayer MoS_2 nanoribbons, *Journal of the American Chemical Society* **136**, 6269 (2014).
- [101] M. Kong, S. Murakami, and T. Zhang, A comprehensive study of complex non-adiabatic exciton dynamics in mosi_2n_4 , *Materials Today Physics* **27**, 100814 (2022).
- [102] H. Yao, C. Zhang, Q. Wang, J. Li, Y. Yu, F. Xu, B. Wang, and Y. Wei, Novel two-dimensional layered MoSi_2Z_4 (Z = P, As): New promising optoelectronic materials, *Nanomaterials* **11**, 559 (2021).
- [103] Q. Wu, L. Cao, Y. S. Ang, and L. K. Ang, Semiconductor-to-metal transition in bilayer MoSi_2N_4 and WSi_2N_4 with strain and electric field, *Applied Physics Letters* **118**, 113102 (2021).
- [104] X. Cai, Z. Zhang, Y. Zhu, L. Lin, W. Yu, Q. Wang, X. Yang, X. Jia, and Y. Jia, A two-dimensional $\text{MoSe}_2/\text{MoSi}_2\text{N}_4$ van der Waals heterostructure with high carrier mobility and diversified regulation of its electronic properties, *Journal of Materials Chemistry C* **9**, 10073 (2021).
- [105] Y. He, Y. H. Zhu, M. Zhang, J. Du, W. H. Guo, S. M. Liu, C. Tian, H. X. Zhong, X. Wang, and J. J. Shi, High hydrogen production in the $\text{InSe}/\text{MoSi}_2\text{N}_4$ van der Waals heterostructure for overall water splitting, *Physical Chemistry Chemical Physics* **24**, 2110 (2022).
- [106] X. Cai, Z. Zhang, A. Song, G. Chen, W. Yu, X. Jia, X. Yang, Y. Liu, and Y. Jia, Indirect to direct bandgap transition and enhanced optoelectronic properties in WSe_2 monolayer through forming $\text{WSe}_2/\text{MoSi}_2\text{N}_4$ bilayer, *SSRN Electronic Journal* (2021).
- [107] C. Q. Nguyen, Y. S. Ang, S. T. Nguyen, N. V. Hoang, N. M. Hung, and C. V. Nguyen, Tunable type-II band alignment and electronic structure of $\text{C}_3\text{N}_4/\text{MoSi}_2\text{N}_4$ heterostructure: Interlayer coupling and electric field, *Physical Review B* **105**, 045303 (2022).
- [108] J. Q. Ng, Q. Wu, L. K. Ang, and Y. S. Ang, Tunable electronic properties and band alignments of $\text{MoSi}_2\text{N}_4/\text{GaN}$ and $\text{MoSi}_2\text{N}_4/\text{ZnO}$ van der Waals heterostructures, *Applied Physics Letters* **120**, 103101 (2022).
- [109] C. Liu, Z. Wang, W. Xiong, H. Zhong, and S. Yuan, Effect of vertical strain and in-plane biaxial strain on type-II $\text{MoSi}_2\text{N}_4/\text{Cs}_3\text{Bi}_2\text{I}_9$ van der Waals heterostructure, *Journal of Applied Physics* **131**, 163102 (2022).
- [110] Y. Guo, J. Min, X. Cai, L. Zhang, C. Liu, and Y. Jia, Two-dimensional type-II BP/ MoSi_2P_4 vdW heterostructures for high-performance solar cells, *Journal of Physical Chemistry C* **126**, 4677 (2022).
- [111] C. Nguyen, N. V. Hoang, H. V. Phuc, A. Y. Sin, and C. V. Nguyen, Two-dimensional boron phosphide/ MoGe_2N_4 van der Waals heterostructure: A promising tunable optoelectronic material, *Journal of Physical Chemistry Letters* **12**, 5076 (2021).
- [112] Q. Liang, X.-y. Luo, Y.-x. Wang, Y.-c. Liang, and Q. Xie, Modulation of Schottky barrier in XSi_2N_4 / graphene (X=Mo and W) heterojunctions by biaxial strain, *Chinese Physics B* **31**, 087101 (2022).
- [113] L. Cao, G. Zhou, Q. Wang, L. K. Ang, and Y. S. Ang, Two-dimensional van der Waals electrical contact to monolayer MoSi_2N_4 , *Applied Physics Letters* **118**, 013106 (2021).
- [114] K. D. Pham, C. Q. Nguyen, C. V. Nguyen, P. V. Cuong, and N. V. Hieu, Two-dimensional van der Waals graphene/transition metal nitride heterostructures as promising high-performance nanodevices, *New Journal of Chemistry* **45**, 5509 (2021).
- [115] N. T. Binh, C. Q. Nguyen, T. V. Vu, and C. V. Nguyen, Interfacial electronic properties and tunable contact types in Graphene/Janus MoGeSiN_4 heterostructures, *Journal of Physical Chemistry Letters* **12**, 3934 (2021).
- [116] C. V. Nguyen, C. Q. Nguyen, S.-T. Nguyen, Y. S. Ang, and N. V. Hieu, Two-dimensional metal/semiconductor contact in a Janus $\text{MoSH}/\text{MoSi}_2\text{N}_4$ van der Waals heterostructure, *Journal of Physical Chemistry Letters* **13**, 2576 (2022).
- [117] D. K. Pham, Electronic properties of a two-dimensional van der Waals $\text{MoGe}_2\text{N}_4/\text{MoSi}_2\text{N}_4$ heterobilayer: Effect of the insertion of a graphene layer and interlayer coupling, *RSC Advances* **11**, 28659 (2021).
- [118] C. Xuefeng, H. Wenna, J. Minglei, R. Fengzhu, P. Chengxiao, G. Qinfen, W. Bing, and Y. Huabing, A direct Z-scheme $\text{MoSi}_2\text{N}_4/\text{BlueP}$ vdW heterostructure for photocatalytic overall water splitting, *Journal of Physics D: Applied Physics* **55**, 215502 (2022).
- [119] A. Bafekry, M. Faraji, A. Abdollahzadeh Ziabari, M. M. Fadlallah, C. V. Nguyen, M. Ghergherehchi, and S. A. Feghhi, A van der Waals heterostructure of $\text{MoS}_2/\text{MoSi}_2\text{N}_4$: A first-principles study, *New Journal of Chemistry* **45**, 8291 (2021).
- [120] J. Wang, X. Zhao, G. Hu, J. Ren, and X. Yuan, Manipulable electronic and optical properties of two-dimensional $\text{MoSTe}/\text{MoGe}_2\text{N}_4$ van der Waals heterostructures, *Nanomaterials* **11**, 3338 (2021).

- [121] A. Yadav, J. Kangsabanik, N. Singh, and A. Alam, Novel two-dimensional MA_2N_4 materials for photovoltaic and spintronic applications, *Journal of Physical Chemistry Letters* **12**, 10120 (2021).
- [122] M. Norouzi Azizabad and H. Alavi-Rad, Quasiparticle and excitonic effects in WSi_2N_4 monolayer, *Physica Scripta* **96**, 125826 (2021).
- [123] Y. Yu, J. Zhou, Z. Guo, and Z. Sun, Novel two-dimensional Janus $MoSiGeN_4$ and $WSiGeN_4$ as highly efficient photocatalysts for spontaneous overall water splitting, *ACS Applied Materials and Interfaces* **13**, 28090 (2021).
- [124] C.-c. Jian, X. Ma, J. Zhang, and X. Yong, Strained $MoSi_2N_4$ monolayers with excellent solar energy absorption and carrier transport properties, *Journal of Physical Chemistry C* **125**, 15185 (2021).
- [125] X. Lv, Y. Xu, B. Mao, G. Liu, G. Zhao, and J. Yang, Strain modulation of electronic and optical properties of monolayer $MoSi_2N_4$, *Physica E: Low-Dimensional Systems and Nanostructures* **135**, 144664 (2022).
- [126] N. Mwankemwa, H.-e. Wang, T. Zhu, Q. Fan, F. Zhang, and W. Zhang, First principles calculations investigation of optoelectronic properties and photocatalytic CO_2 reduction of $(MoSi_2N_4)_{5-n}/(MoSiGeN_4)_n$ in-plane heterostructures, *Results in Physics* **37**, 105549 (2022).
- [127] A. Bafekry, C. Stampfl, M. Naseri, M. M. Fadlallah, M. Faraji, M. Ghergherehchi, D. Gogova, and S. A. Feghhi, Effect of electric field and vertical strain on the electro-optical properties of the $MoSi_2N_4$ bilayer: A first-principles calculation, *Journal of Applied Physics* **129**, 155103 (2021).
- [128] J. Xu, Q. Wu, Z. Sun, N. Mwankemwa, W. bin Zhang, and W. xing Yang, First-principles investigations of electronic, optical, and photocatalytic properties of Au-adsorbed $MoSi_2N_4$ monolayer, *Journal of Physics and Chemistry of Solids* **162**, 110494 (2022).
- [129] Z. Sun, J. Xu, N. Mwankemwa, W. Yang, X. Wu, Z. Yi, S. Chen, and W. Zhang, Alkali-metal (Li, Na, and K)-adsorbed $MoSi_2N_4$ monolayer: An investigation of its outstanding electronic, optical, and photocatalytic properties, *Communications in Theoretical Physics* **74**, 015503 (2022).
- [130] R. Chen, D. Chen, and W. Zhang, First-principles calculations to investigate stability, electronic and optical properties of fluorinated $MoSi_2N_4$ monolayer, *Results in Physics* **30**, 104864 (2021).
- [131] J. Zeng, L. Xu, Y. Yang, X. Luo, H. J. Li, S. X. Xiong, and L. L. Wang, Boosting the photocatalytic hydrogen evolution performance of monolayer C_2N coupled with $MoSi_2N_4$: Density-functional theory calculations, *Physical Chemistry Chemical Physics* **23**, 8318 (2021).
- [132] J. Chen and Q. Tang, The versatile electronic, magnetic and photo-electro catalytic activity of a new 2D MA_2Z_4 Family, *Chemistry - A European Journal* **27**, 9925 (2021).
- [133] C. Formed, J.-k. Yoon, K.-h. Lee, S. B. Touski, J. Xu, X. Mao, and Z.-h. Xie, Band-gap engineering, magnetic behavior and Dirac-semimetal character in the $MoSi_2N_4$ nanoribbon with armchair and zigzag edges, *Journal of Physics D: Applied Physics* **55**, 035301 (2022).
- [134] Y. Ding and Y. Wang, First-principles study of two-dimensional $MoN_2X_2Y_2$ ($X=B-In$, $Y=N-Te$) nanosheets: The III-VI analogues of $MoSi_2N_4$ with peculiar electronic and magnetic properties, *Applied Surface Science* **593**, 153317 (2022).
- [135] Y. Feng, Z. Wang, X. Zuo, and G. Gao, Electronic phase transition, spin filtering effect, and spin Seebeck effect in 2D high-spin-polarized VSi_2X_4 ($X=N, P, As$), *Applied Physics Letters* **120**, 092405 (2022).
- [136] D. Dey, A. Ray, and L. Yu, Intrinsic ferromagnetism and restrictive thermodynamic stability in MA_2N_4 and Janus $VSiGeN_4$ monolayers, *arXiv:2203.11605* (2022).
- [137] X. L. Wang, Dirac spin-gapless semiconductors: Promising platforms for massless and dissipationless spintronics and new (quantum) anomalous spin Hall effects, *National Science Review* **4**, 252 (2017).
- [138] X. Wang, T. Li, Z. Cheng, X. L. Wang, and H. Chen, Recent advances in Dirac spin-gapless semiconductors, *Applied Physics Reviews* **5**, 041103 (2018).
- [139] Q. Cui, Y. Zhu, J. Liang, P. Cui, and H. Yang, Spin-valley coupling in a two-dimensional VSi_2N_4 monolayer, *Physical Review B* **103**, 085421 (2021).
- [140] M. R. K. Akanda and R. K. Lake, Magnetic properties of $MoSi_2N_4$, VSi_2N_4 , and VSi_2P_4 monolayers, *Applied Physics Letters* **119**, 052402 (2021).
- [141] M. Xue, W. He, Q. Gong, M. Yi, and W. Guo, Nonlinear elasticity and strain-tunable magnetocalorics of antiferromagnetic monolayer mnp_3 , *Extreme Mechanics Letters* , 101900 (2022).
- [142] L. Webster and J. A. Yan, Strain-tunable magnetic anisotropy in monolayer $CrCl_3$, $CrBr_3$, and CrI_3 , *Physical Review B* **98**, 144411 (2018).
- [143] S. Zheng, C. Huang, T. Yu, M. Xu, S. Zhang, H. Xu, Y. Liu, E. Kan, Y. Wang, and G. Yang, High-temperature ferromagnetism in an Fe_3P monolayer with a large magnetic anisotropy, *Journal of Physical Chemistry Letters* **10**, 2733 (2019).
- [144] H. L. Zhuang, P. R. Kent, and R. G. Hennig, Strong anisotropy and magnetostriction in the two-dimensional Stoner ferromagnet Fe_3GeTe_2 , *Physical Review B* **93**, 134407 (2016).
- [145] H. Han, H. Zheng, Q. Wang, and Y. Yan, Enhanced magnetic anisotropy and Curie temperature of the NiI_2 monolayer by applying strain: A first-principles study, *Physical Chemistry Chemical Physics* **22**, 26917 (2020).
- [146] E. Torun, H. Sahin, C. Bacaksiz, R. T. Senger, and F. M. Peeters, Tuning the magnetic anisotropy in single-layer crystal structures, *Physical Review B* **92**, 104407 (2015).
- [147] B. Huang, G. Clark, E. Navarro-Moratalla, D. R. Klein, R. Cheng, K. L. Seyler, D. Zhong, E. Schmidgall, M. A. McGuire, D. H. Cobden, W. Yao, D. Xiao, P. Jarillo-Herrero, and X. Xu, Layer-dependent ferromagnetism in a van der Waals crystal down to the monolayer limit, *Nature* **546**, 270 (2017).
- [148] Z. Fei, B. Huang, P. Malinowski, W. Wang, T. Song, J. Sanchez, W. Yao, D. Xiao, X. Zhu, A. F. May, W. Wu, D. H. Cobden, J. H. Chu, and X. Xu, Two-dimensional itinerant ferromagnetism in atomically thin Fe_3GeTe_2 , *Nature Materials* **17**, 778 (2018).
- [149] J. Y. You, Z. Zhang, X. J. Dong, B. Gu, and G. Su, Two-dimensional magnetic semiconductors with room Curie temperatures, *Physical Review Research* **2**, 013002 (2020).
- [150] Z. Jiang, P. Wang, J. Xing, X. Jiang, and J. Zhao, Screening and design of novel 2D ferromagnetic materials with high Curie temperature above room temperature,

- ACS Applied Materials and Interfaces **10**, 39032 (2018).
- [151] Y. Li, J. Wang, G. Yang, and Y. Liu, Strain-induced magnetism in MSi_2N_4 ($M = \text{V}, \text{Cr}$): A first-principles study, *Annalen der Physik* **533**, 2100273 (2021).
- [152] A. Ray, S. Tyagi, N. Singh, and U. Schwingenschlöggl, Inducing half-metallicity in monolayer MoSi_2N_4 , *ACS Omega* **6**, 30371 (2021).
- [153] M. A. Abdelati, A. A. Maarouf, and M. M. Fadlallah, Substitutional transition metal doping in MoSi_2N_4 monolayer: Structural, electronic and magnetic properties, *Physical Chemistry Chemical Physics* **24**, 3035 (2022).
- [154] M. Yi, B. X. Xu, R. Müller, and D. Gross, Strain-mediated magnetoelectric effect for the electric-field control of magnetic states in nanomagnets, *Acta Mechanica* **230**, 1247 (2019).
- [155] D. Sander, The correlation between mechanical stress and magnetic anisotropy in ultrathin films, *Reports on Progress in Physics* **62**, 809 (1999).
- [156] Q. Gong, M. Yi, and B. X. Xu, Electric field induced magnetization reversal in magnet/insulator nanoheterostructure, *International Journal of Smart and Nano Materials* **11**, 298 (2020).
- [157] I. J. Park, S. Kwon, and R. K. Lake, Effects of filling, strain, and electric field on the Néel vector in antiferromagnetic CrSb , *Physical Review B* **102**, 224426 (2020).
- [158] J. Yuan, Q. Wei, M. Sun, X. Yan, Y. Cai, L. Shen, and U. Schwingenschlöggl, Protected valley states and generation of valley- and spin-polarized current in monolayer MA_2Z_4 , *Physical Review B* **105**, 195151 (2022).
- [159] Z. Cui, K. Yang, K. Ren, S. Zhang, and L. Wang, Adsorption of metal atoms on MoSi_2N_4 monolayer: A first principles study, *Materials Science in Semiconductor Processing* **152**, 107072 (2022).
- [160] B. Li, J. Geng, H. Ai, Y. Kong, H. Bai, K. H. Lo, K. W. Ng, Y. Kawazoe, and H. Pan, Design of 2D materials- $\text{MSi}_2\text{C}:\text{XN}_{4-x}$ ($M = \text{Cr}, \text{Mo}$, and W ; $X=1$ and 2)-with tunable electronic and magnetic properties, *Nanoscale* **13**, 8038 (2021).
- [161] S. Li, W. Wu, X. Feng, S. Guan, W. Feng, Y. Yao, and S. A. Yang, Valley-dependent properties of monolayer MoSi_2N_4 , WSi_2N_4 , and MoSi_2As_4 , *Physical Review B* **102**, 235435 (2020).
- [162] H. Ai, D. Liu, J. Geng, S. Wang, K. H. Lo, and H. Pan, Theoretical evidence of the spin-valley coupling and valley polarization in two-dimensional MoSi_2X_4 ($X = \text{N}, \text{P}$, and As), *Physical Chemistry Chemical Physics* **23**, 3144 (2021).
- [163] Y. Liu, T. Zhang, K. Dou, W. Du, R. Peng, Y. Dai, B. Huang, and Y. Ma, Valley-contrasting physics in single-layer CrSi_2N_4 and CrSi_2P_4 , *Journal of Physical Chemistry Letters* **12**, 8341 (2021).
- [164] G. Hussain, A. Samad, M. Ur Rehman, G. Cuono, and C. Autieri, Emergence of rashba splitting and spin-valley properties in janus $\text{mogesip}_2\text{as}_2$ and $\text{wgesip}_2\text{as}_2$ monolayers, *Journal of Magnetism and Magnetic Materials* **563**, 169897 (2022).
- [165] S. Sheoran, D. Gill, A. Phutela, and S. Bhattacharya, Coupled spin-valley, Rashba effect and hidden persistent spin polarization in WSi_2N_4 family, [arXiv:2208.00127](https://arxiv.org/abs/2208.00127) (2022).
- [166] C. Yang, Z. Song, X. Sun, J. Lu, L. Berkeley, and O. P. Materials, Valley pseudospin in monolayer MoSi_2N_4 and MoSi_2As_4 , *Physical Review B* **103**, 035308 (2020).
- [167] X. Feng, X. Xu, Z. He, R. Peng, Y. Dai, B. Huang, and Y. Ma, Valley-related multiple Hall effect in monolayer VSi_2P_4 , *Physical Review B* **104**, 075421 (2021).
- [168] S. Li, Q. Wang, C. Zhang, P. Guo, and S. A. Yang, Correlation-driven topological and valley states in monolayer VSi_2P_4 , *Physical Review B* **104**, 085149 (2021).
- [169] Y. Wang and Y. Ding, Switchable valley polarization and quantum anomalous Hall state in the $\text{VN}_2\text{X}_2\text{Y}_2$ nanosheets ($X = \text{group-III}$ and $Y = \text{group-VI}$ elements), *Applied Physics Letters* **119**, 193101 (2021).
- [170] R. Islam, R. Verma, B. Ghosh, Z. Muhammad, A. Bansil, C. Autieri, and B. Singh, Switchable large-gap quantum spin Hall state in two-dimensional MSi_2Z_4 materials class, [arXiv:2207.08407](https://arxiv.org/abs/2207.08407) (2022).
- [171] X. Sun, Z. Song, N. Huo, S. Liu, C. Yang, J. Yang, W. Wang, and J. Lu, Performance limit of monolayer MoSi_2N_4 transistors, *Journal of Materials Chemistry C* **9**, 14683 (2021).
- [172] J. Huang, P. Li, X. Ren, and Z. X. Guo, Promising properties of a sub-5-nm monolayer MoSi_2N_4 transistor, *Physical Review Applied* **16**, 044022 (2021).
- [173] B. Ye, X. Jiang, Y. Gu, G. Yang, Y. Liu, H. Zhao, X. Yang, C. Wei, X. Zhang, and N. Lu, Quantum transport of short-gate MOSFETs based on monolayer MoSi_2N_4 , *Physical Chemistry Chemical Physics* **24**, 6616 (2022).
- [174] N. Ghobadi, M. Hosseini, and S. B. Touski, Field-effect transistor based on MoSi_2N_4 and WSi_2N_4 monolayers under biaxial strain: A computational study of the electronic properties, *IEEE Transactions on Electron Devices* **69**, 863 (2022).
- [175] K. Nandan, G. S. Member, B. Ghosh, A. Agarwal, and S. Bhowmick, Two-dimensional MoSi_2N_4 : An excellent 2-D semiconductor for field-effect transistors, *IEEE Transactions on Electron Devices* **69**, 406 (2022).
- [176] H. Zhang, B. Shi, L. Xu, J. Yan, W. Zhao, Z. Zhang, Z. Zhang, and J. Lu, Sub-5 nm monolayer MoS_2 transistors toward low-power devices, *ACS Applied Electronic Materials* **3**, 1560 (2021).
- [177] S. Zhu and D. Wang, Photocatalysis: Basic principles, diverse forms of implementations and emerging scientific opportunities, *Advanced Energy Materials* **7**, 1700841 (2017).
- [178] Y. Li, C. Gao, R. Long, and Y. Xiong, Photocatalyst design based on two-dimensional materials, *Materials Today Chemistry* **11**, 197 (2019).
- [179] W. Shi, G. Yin, S. Yu, T. Hu, and X. Wang, Atomic precision tailoring of two-dimensional MoSi_2N_4 as electrocatalyst for hydrogen evolution reaction, *Journal of Materials Science* (2022).
- [180] J. Zhao, Y. Zhao, H. He, P. Zhou, Y. Liang, and T. Frauenheim, Stacking engineering: A boosting strategy for 2D photocatalysts, *Journal of Physical Chemistry Letters* **12**, 10190 (2021).
- [181] G. Hussain, M. Manzoor, M. W. Iqbal, I. Muhammad, A. Bafekry, H. Ullah, and C. Autieri, Strain modulated electronic and optical properties of laterally stitched $\text{MoSi}_2\text{N}_4/\text{XSi}_2\text{N}_4$ ($X=\text{W}, \text{Ti}$) 2D heterostructures, *Physica E: Low-dimensional Systems and Nanostructures* **144**, 1154 (2022).
- [182] Y. T. Ren, L. Hu, Y. T. Chen, Y. J. Hu, J. L. Wang, P. L. Gong, H. Zhang, L. Huang, and X. Q. Shi, Two-dimensional MSi_2N_4 monolayers

- and van der Waals heterostructures: Promising spintronic properties and band alignments, *Physical Review Materials* **6**, 064006 (2022).
- [183] Y. Zang, Q. Wu, W. Du, Y. Dai, B. Huang, and Y. Ma, Activating electrocatalytic hydrogen evolution performance of two-dimensional MSi_2N_4 ($\text{M}=\text{Mo}, \text{W}$): A theoretical prediction, *Physical Review Materials* **5**, 045801 (2021).
- [184] W. Qian, Z. Chen, J. Zhang, and L. Yin, Monolayer $\text{MoSi}_2\text{N}_{4-x}$ as promising electrocatalyst for hydrogen evolution reaction: A DFT prediction, *Journal of Materials Science and Technology* **99**, 215 (2022).
- [185] C. Xiao, R. Sa, Z. Cui, S. Gao, W. Du, X. Sun, X. Zhang, Q. Li, and Z. Ma, Enhancing the hydrogen evolution reaction by non-precious transition metal (Non-metal) atom doping in defective MoSi_2N_4 monolayer, *Applied Surface Science* **563**, 150388 (2021).
- [186] Y. Luo, M. Li, Y. Dai, X. Zhang, R. Zhao, F. Jiang, C. Ling, and Y. Huang, Screening of effective NRR electrocatalysts among the Si-based MSi_2N_4 ($\text{M} = \text{Ti}, \text{Zr}, \text{Hf}, \text{V}, \text{Nb}, \text{Ta}, \text{Cr}, \text{Mo}, \text{and W}$) monolayers, *Journal of Materials Chemistry A* **9**, 15217 (2021).
- [187] S. Lu, Y. Zhang, F. Lou, K. Guo, and Z. Yu, Non-precious metal activated MoSi_2N_4 monolayers for high-performance OER and ORR electrocatalysts: A first-principles study, *Applied Surface Science* **579**, 152234 (2022).
- [188] M. R. Sahoo, A. Ray, and N. Singh, Theoretical insights into the hydrogen evolution reaction on VGe_2N_4 and NbGe_2N_4 monolayers, *ACS Omega* **7**, 7837 (2022).
- [189] Y. Liu, Y. Ji, and Y. Li, Multilevel theoretical screening of novel two-dimensional MA_2Z_4 family for hydrogen evolution, *Journal of Physical Chemistry Letters* **12**, 9149 (2021).
- [190] J. Zheng, X. Sun, J. Hu, S. Wang, Z. Yao, S. Deng, X. Pan, Z. Pan, and J. Wang, Symbolic transformer accelerating machine learning screening of hydrogen and deuterium evolution reaction catalysts in MA_2Z_4 materials, *ACS Applied Materials and Interfaces* **13**, 50878 (2021).
- [191] Y. Chen, S. Tian, and Q. Tang, First-principles studies on electrocatalytic activity of novel two-dimensional MA_2Z_4 monolayers toward oxygen reduction reaction, *Journal of Physical Chemistry C* **125**, 22581 (2021).
- [192] C. Lin, X. Feng, D. Legut, X. Liu, Z. W. Seh, R. Zhang, and Q. Zhang, Discovery of efficient visible-light driven oxygen evolution photocatalysts: Automated high-throughput computational screening of MA_2Z_4 , *Advanced Functional Materials*, 2207415 (2022).
- [193] Z. Wang, G. Zhang, Y. Wang, C. Huang, Y. Liu, C. Ouayng, and J. Hu, Heavy 2D VSi_2N_4 : High capacity and full battery open-circuit voltage as Li/Na-ion batteries anode, *Applied Surface Science* **593**, 153354 (2022).
- [194] X. M. Li, Z. Z. Lin, L. R. Cheng, and X. Chen, Layered MoSi_2N_4 as electrode material of Zn–Air battery, *Physica Status Solidi - Rapid Research Letters* **16**, 2200007 (2022).
- [195] R. E. Munteanu, P. S. Moreno, M. Bramini, and S. Gáspár, 2D materials in electrochemical sensors for in vitro or in vivo use, *Analytical and Bioanalytical Chemistry* **413**, 701 (2020).
- [196] D. J. Buckley, N. C. Black, E. G. Castanon, C. Melios, M. Hardman, and O. Kazakova, Frontiers of graphene and 2D material-based gas sensors for environmental monitoring, *2D Materials* **7**, 032002 (2020).
- [197] D. Tyagi, H. Wang, W. Huang, L. Hu, Y. Tang, Z. Guo, Z. Ouyang, and H. Zhang, Recent advances in two-dimensional-material-based sensing technology toward health and environmental monitoring applications, *Nanoscale* **12**, 3535 (2020).
- [198] K. Li, W. Yang, M. Yi, and Z. Shen, Graphene-based pressure sensor and strain sensor for detecting human activities, *Smart Materials and Structures* **30**, 085027 (2021).
- [199] B. B. Subbanna, K. Choudhary, S. Singh, and S. Kumar, 2D material-based optical sensors: a review, *ISSS Journal of Micro and Smart Systems* **11**, 169 (2022).
- [200] A. Bafekry, M. Faraji, M. M. Fadlallah, A. Abdolazadeh Ziabari, A. Bagheri Khatibani, S. A. Feghhi, M. Ghergherehchi, and D. Gogova, Adsorption of habitat and industry-relevant molecules on the MoSi_2N_4 monolayer, *Applied Surface Science* **564**, 150326 (2021).